Florian Apolloner, BSc

Determination of selective adsorption resonance lifetimes on He-Sb(111)

MASTER THESIS

For obtaining the academic degree

Diplom-Ingenieur

Master Programme of

Technical Physics

Graz University of Technology

Supervisor:

Univ.-Prof. Dipl.-Phys. Dr.rer.nat. Wolfgang E. Ernst

Institute of Experimental Physics

Graz, February 2015

This document is set in Palatino, compiled with pdfLaTeX2e and `Biber`.

The LaTeX template from Karl Voit is based on KOMA script and can be found online: https://github.com/novoid/LaTeX-KOMA-template

EIDESSTATTLICHE ERKLÄRUNG

AFFIDAVIT

Ich erkläre an Eides statt, dass ich die vorliegende Arbeit selbstständig verfasst, andere als die angegebenen Quellen/Hilfsmittel nicht benutzt, und die den benutzten Quellen wörtlich und inhaltlich entnommenen Stellen als solche kenntlich gemacht habe. Das in TUGRAZonline hochgeladene Textdokument ist mit der vorliegenden Masterarbeit/Diplomarbeit/Dissertation identisch.

I declare that I have authored this thesis independently, that I have not used other than the declared sources/resources, and that I have explicitly indicated all material which has been quoted either literally or by content from the sources used. The text document uploaded to TUGRAZonline is identical to the present master's thesis/diploma thesis/doctoral dissertation.

_____ _____

Datum / Date Unterschrift / Signature

Kurzfassung

An Kristalloberflächen wird die Symmetrie abrupt unterbrochen, was sowohl zu einer Änderung der Zahl der Bindungspartner, als auch zu einer Beeinflussung der Kraftverhältnisse und elektronischen Eigenschaften führt. Dies kann zu neuen Eigenschaften führen, die sich deutlich von denen des Bulk unterscheiden. Aufgrund der Wichtigkeit von Oberflächen für Forschungsfelder wie topologische Isolatoren und Nanofilme ist ein weitreichendes Verständnis dieser von großer Bedeutung.

Aus den verfügbaren Möglichkeiten für Oberflächenuntersuchungen kann sich die Heliumatomstreuung besonders hervorheben, da sie nicht nur zerstörungsfrei sondern auch rein oberflächensensitiv ist. Mithilfe dieser Technik sind nicht nur Strukturaufklärungen der Oberfläche möglich, sondern können auch Informationen über die Oberflächendynamik und das Interaktionspotential zwischen den Heliumatomen und der Oberfläche gewonnen werden.

Im Zuge der Datenauswertung müssen einige Spezialeffekte berücksichtigt werden, unter anderem *selective adsorption resonances* (SAR), wobei hier das Heliumatom in einen gebundenen Zustand des Interaktionspotentiales übergeht. In dieser Arbeit werden die Lebenszeiten dieser SAR auf Sb(111) untersucht. Anschließend folgt ein Vergleich mit zwei theoretischen Modellen, einerseits nach Fermis Goldener Regel und andererseits durch eine Simulation des

Experiments. Für Letztere wurde die existierende Implementierung eines *Close-Coupling* Algorithmus neu geschrieben und auf Geschwindigkeit optimiert.

Zusätzlich wurde ein neues Web-basiertes Überwachungssystem für den Messapparat implementiert. Dieses erlaubt einerseits die Überwachung aller Sensorwerte, als auch die Einstellung von Prozesswerten und eine Alarmfunktion, falls Sensorwerte vordefinierte Bereiche verlassen.

Abstract

At the surfaces of crystals the symmetry is suddenly broken, leading to an alteration of the number of bonding partners, as well as change in the force constants and electronic states. Those changes can lead to new properties compared to the bulk properties. As surfaces are very important for many research fields including topological insulators and nanofilms, a deep understanding of surface properties and their dynamics is of major importance.

Within the available options for surface investigations, helium atom scattering can position itself as a unique tool as it is not only nondestructive but also completely surface sensitive. Using this technique, it is not only possible to obtain information about the surface structure, but also about its dynamics and the interaction potential between the helium atoms and the investigated surface.

As part of the data analysis, several special effects have to be considered. Among them are *selective adsorption resonances* (SAR) where the helium atom adsorbs into a bound state of the surface interaction potential. In this work the lifetime of these SAR on Sb(111) are determined. They are then compared to two theoretical models, a golden rule treatment and a simulation of the experiment. For the simulation the existing implementation of a *Close Coupling* algorithm was rewritten and optimized for speed.

Additionally a new web-based monitoring system for the apparatus was written, which allows remote monitoring as well as configuration of sensor target values and alarm functionality if the values are outside of specified operational ranges.

Contents

List of Figures

1 Introduction

For decades *Helium Atom Scattering* (HAS) has been the tool of choice when it comes to surface sensitive, and nondestructive investigations[1,2]. As the low-energy helium atoms are repelled by very low surface electron charge densities already and never reach the first layer of atoms, all information gathered in experiments has to be a result of the interaction between the helium atom and the surface electrons.

Not only does HAS provide insights into the structural properties of the investigated surface[3], but it also provides the means to investigate the surface dynamics[4] as well as the interaction potential between the helium and the probed surface[5,6].

To be able to analyze the measured data at hand exactly, a lot of special effects and their ramifications have to be considered[7,8]. Among those effects are *selective adsorption resonances* (SAR), where the helium atom undergoes a transition into a bound state of the interaction potential. The longer the helium atom remains in this bound state on the surface, the higher the interaction probabilities with the electron charge density are, possibly leading to an amplification of otherwise unobservable effects[9]. Therefore it is important to know which bound states have a long lifetime and can be utilized for the amplification.

Antimony is an interesting material to investigate with HAS. While being a metalloid in the bulk, it exhibits metallic character on the surface and serves as one of the main ingredients for topological insulators[10,11]. Furthermore, antimony nanofilms are a promising candidates in spintronics, due to their tunable band gap and reverse spin polarization[12,13].

2 Theoretical Background

2.1 Surface Description

Throughout this work surfaces will be investigated using HAS. Therefore a short introduction of the description of surfaces is given in this section.

2.1.1 Crystal Structure

A crystal is a solid material whose constituents form a periodic structure. This means that the whole crystal can be viewed as an endless repetition of atom groups which are called the *basis*. The *basis* is attached to a *lattice* as shown in figure 2.1.

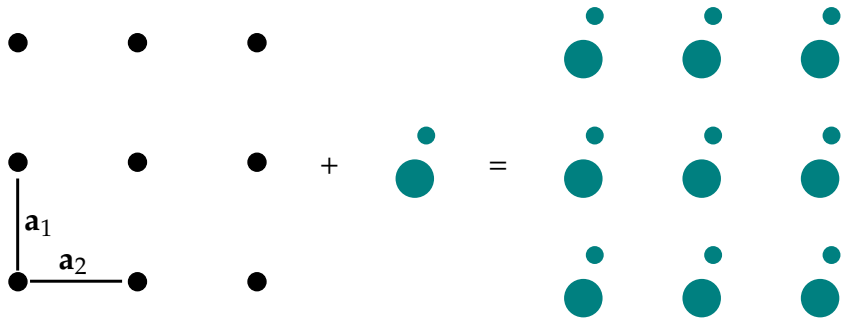

Figure 2.1: Visualization of the *lattice*, *basis* and the attachment of the *basis* to the *lattice*.

Lattice points are connected via the translation vectors $\mathbf{a}_1$, $\mathbf{a}_2$ and $\mathbf{a}_3$. As a consequence of the periodicity all points $\mathbf{r}'$, from which the arrangement of the crystal looks as in point $\mathbf{r}$, can be described as

$$\mathbf{r}' = \mathbf{r} + n_1\mathbf{a}_1 + n_2\mathbf{a}_2 + n_3\mathbf{a}_3, \tag{2.1}$$

with n_i being integers. If there is no other set of translation vectors with a volume less than $\mathbf{a}_1 \cdot (\mathbf{a}_2 \times \mathbf{a}_3)$ while still filling the crystal completely then the vectors $\mathbf{a}_i$ are called *primitive lattice vectors*. These primitive lattice vectors form the *primitive unit cell*. One way to easily construct such a minimal volume cell is by constructing a *Wigner-Seitz cell* as follows:

- Choose a lattice point and connect it to its neighbors using straight lines.
- Draw planes (or lines in two dimensions) perpendicular to the lines through their center point.
- The smallest volume (or area in two dimensions) enclosed by those planes (or lines) is then the Wigner-Seitz cell.

The possible arrangements of the primitive translation vectors into so called "Bravais lattices" is limited to five in two dimensions and 14 in three dimensions[14].

To describe the crystal completely, the position $\mathbf{r}$ of an atom within its lattice cell is then written as

$$\mathbf{r} = t_1\mathbf{a}_1 + t_2\mathbf{a}_2 + t_3\mathbf{a}_3. \tag{2.2}$$

Here t_i is between zero and one. Given (2.1) and (2.2), one can describe the position of any atom in the crystal.

2.1.2 Surface Structure

While infinite crystals are a nice construct, in reality one inevitably has to deal with surfaces. Similar to the bulk, the structure is described via a basis and lattice in two dimensions:

$$\mathbf{R}' = \mathbf{R} + n_1\mathbf{A}_1 + n_2\mathbf{A}_2 \tag{2.3}$$

$$\mathbf{R} = t_1\mathbf{A}_1 + t_2\mathbf{A}_2. \tag{2.4}$$

Following existing conventions, the nomenclature of Cabrera et al.[15] is adapted here. In this nomenclature all vectors in the surface plane are written in capital letters. Three dimensional vectors derived from those surface vectors are often written as $\mathbf{r} = (\mathbf{R}, z)$.

Although this already allows one to describe the structure of the surface, there is no indication how this surface plane is oriented with respect to the bulk. Therefore the planes are described using Miller indices which are constructed as follows:

- The intersections with the axes spanned by $\mathbf{a}_i$ are determined, eg $3\mathbf{a}_1$, $2\mathbf{a}_2$ and $2\mathbf{a}_3$.
- A vector normal to the plane is constructed by taking the reciprocals of these numbers, leading to $\frac{1}{3}$, $\frac{1}{2}$ and $\frac{1}{2}$.
- Multiplying with the lowest common multiple yields the final Miller index of $(2,3,3)$.

Symmetry equivalent planes to $(2,3,3)$ are then written as $\{2,3,3\}$. Planes parallel to an axis have a zero in the corresponding position as shown in figure 2.2. Negative indices are written with a bar over the numbers instead of a minus sign in front of them.

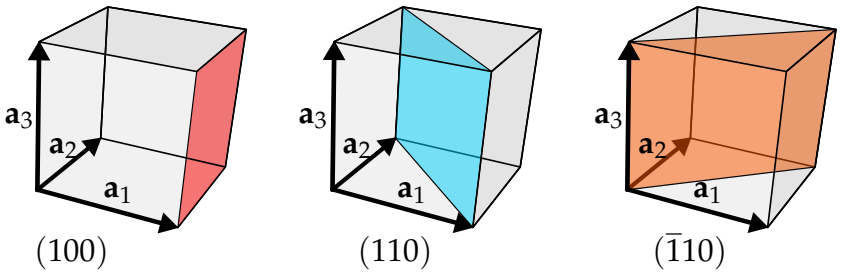

Figure 2.2: Illustration of planes specified by Miller indices. Original figure by Felix Kling, adapted from `https://en.wikipedia.org/wiki/File:Miller_Indices_Felix_Kling.svg`

2.1.3 Reciprocal Space

To describe scattering experiments the *reciprocal lattice* is used. The reciprocal lattice resides in reciprocal space, also named *momentum space*, and is obtained via a Fourier transform from real space. The Wigner-Seitz cell in reciprocal space is called Brillouin zone. To obtain the reciprocal base vectors the following formulas can be used to obtain them from their real space counter parts:

$$(\mathbf{B}_1, \mathbf{b}_{1,z}) = \mathbf{b}_1 = 2\pi \frac{\mathbf{a}_2 \times \mathbf{n}}{\mathbf{a}_1 (\mathbf{a}_2 \times \mathbf{n})} \tag{2.5}$$

$$(\mathbf{B}_2, \mathbf{b}_{2,z}) = \mathbf{b}_2 = 2\pi \frac{\mathbf{n} \times \mathbf{a}_1}{\mathbf{a}_1 (\mathbf{a}_2 \times \mathbf{n})}. \tag{2.6}$$

Here, a surface plane parallel to the plane spanned by the vectors $\mathbf{a}_1$ and $\mathbf{a}_2$ was chosen and the third vector was replaced with $\mathbf{n}$, the unit vector normal to the investigated surface. Following this, a general translation vector in reciprocal space can be written as

$$\mathbf{G}_{h,k} = h\mathbf{B}_1 + k\mathbf{B}_2, \tag{2.7}$$

with h and k as integers.

2.2 Properties and Structure of the Sb(111) Surface

Antimony is a metalloid and located in the fifth group and fifth period of the periodic table with an atomic number of 51. It exhibits metallic properties on the surface and is one of the main ingredients for topological insulators[10,11]. As nanofilm it undergoes topoeletronic phase transitions depending on the thickness of the film[12]. Due to the tunable band gap and reverse spin polarization, Sb(111) nanofilms are promising candidates for spintronic applications[13]. Given those features, HAS-based surface analysis is a perfect method to complement the existing investigations of electronic surface states. Throughout

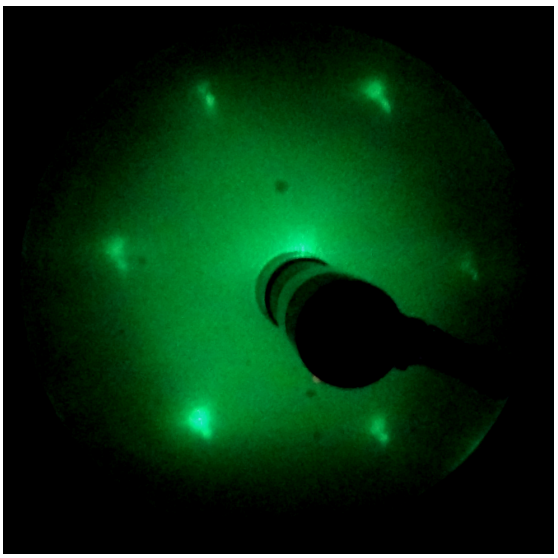

Figure 2.3: LEED picture of the Sb(111) surface in the high symmetry direction $\overline{\Gamma M}$. The colors have been enhanced using the *GNU Image Manipulation Program* (GIMP).

our experiments pure antimony was used as sample. In the bulk it crystallizes in a rhombohedral A7 structure[16] and has two atoms per unit cell. As other

pnictogens, antimony has a puckered bilayer structure perpendicular to the <111>-direction. The bonding type is covalent within a bilayer and van der Waals like between the bilayers. The forces between the bilayers are slightly weaker, which allows easy cleaving of the crystal perpendicular to the <111>-direction. The puckered bilayer structure, along with its lattice distances is depicted in figure 2.4(b). The cleaved surface exhibits a hexagonal structure, which can be verified by *LEED* (low-energy-electron-diffraction) as shown in figure 2.3. When the electron energy is increased to a point where they can penetrate below the first layer of atoms, the structure reduces to a three-fold symmetry as the second layer of atoms from the first bilayer become now relevant. For the energy range of HAS experiments, though, the crystal can be considered as six-fold symmetric (compare with figure 2.4(a) for a top view of the structure).

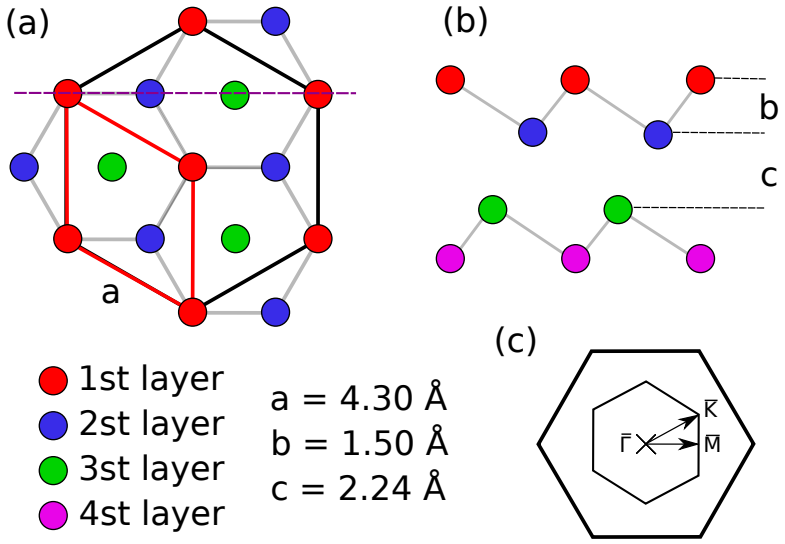

Figure 2.4: Diagram depicting the surface structure of Sb(111). (a) Top view onto the crystal, the first layer atoms form a hexagonal structure. (b) Side view with the first and second bilayer, showing the difference in lattice distances. (c) First Brillouin zone, with the high symmetry directions for a six-fold symmetric structure.

2.3 Lattice Vibrations and Phonons

Lattice vibrations are fundamental in any crystal and usually described by quasiparticles, the so called phonons. Phonons are quanta of vibrational motions at a specific frequency. The lattice dynamics as a whole can then be described as superposition of those single phonons. The simplest possible

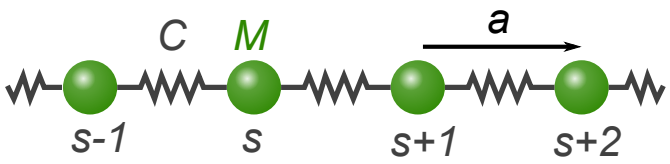

Figure 2.5: 1-dimensional chain of atoms connected by Hookean springs.

crystal imaginable is a one-dimensional chain of atoms. As long as all of the atoms are in their respective equilibrium position, there is no force on the atoms. If one atom is moved, the neighboring atoms are exposed to a force, moving them out of their equilibrium position, too, and in turn, those atoms again induce a motion in their neighbors, effectively resulting in a motion of the whole crystal. This system can be described as a chain of atoms (compare with figure 2.5) connected by Hookean springs with the spring constant C, as long as the displacements are small. With those conditions in mind, the force F_s on an atom at lattice position index s and a displacement of u_s can be written as:

$$F_s = C(u_{s+1} - u_s) - C(u_s - u_{s-1}). \tag{2.8}$$

Following Newton's laws, the equation of motion for an atom with mass M is

$$M\frac{d^2u_s}{dt^2} = C(u_{s+1} + u_{s-1} - 2u_s), \tag{2.9}$$

which can be solved by assuming plane wave solutions of the form

$$u_s(t) = u \cdot e^{i(q \cdot sa - \omega t)}. \tag{2.10}$$

Here a is the spacing of the atom in the equilibrium position and q the wave vector of the phonon. Substituting this solution into equation (2.9) a dispersion relation $\omega(q)$ is derived:

$$\omega(q) = \sqrt{\frac{4C}{M}} \left| \sin\left(\frac{qa}{2}\right) \right|. \tag{2.11}$$

This dispersion starts linearly for small wave vectors, resulting in a constant group velocity in the long wave limit. It reaches its maximum at the zone boundary $\frac{\pi}{a}$ and goes back to zero at the reciprocal lattice constant $b = \frac{2\pi}{a}$. The dispersion then continues with a periodicity equal to the reciprocal lattice constant. Therefore all relevant information is contained in the first Brillouin zone. In general this model is too simple to describe the lattice dynamics of

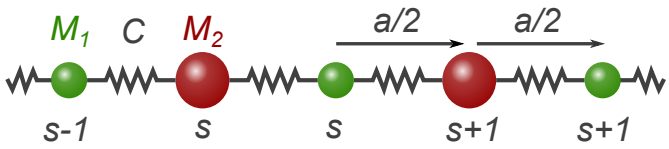

Figure 2.6: 1-dimensional chain of atoms with different masses connected by Hookean springs.

a crystal. A better model is obtained by assuming different force constants between the atoms or assuming different masses for the atoms in the unit cell, as shown in figure 2.6. Those two approaches are mathematically equivalent. For simplicity in the equations, different masses will be assumed in the following derivation. The two masses now lead to a set of coupled equations:

$$M_1 \frac{d^2 u_s}{dt^2} = C(w_s + w_{s-1} - 2u_s) \tag{2.12}$$

$$M_2 \frac{d^2 w_s}{dt^2} = C(u_{s+1} + u_s - 2w_s). \tag{2.13}$$

Using the same plane wave solutions as before and solving the equations gives rise to two dispersion branches, namely an *acoustic* (ω_-) and an *optical* branch (ω_+).

$$\omega_\pm^2 = C\left[\left(\frac{1}{M_1}+\frac{1}{M_2}\right) \pm \sqrt{\left(\frac{1}{M_1}+\frac{1}{M_2}\right)^2 - \frac{4}{M_1 M_2}\sin^2\left(\frac{qa}{2}\right)}\right]. \tag{2.14}$$

The result is depicted in figure 2.7, the acoustic branch roughly corresponds

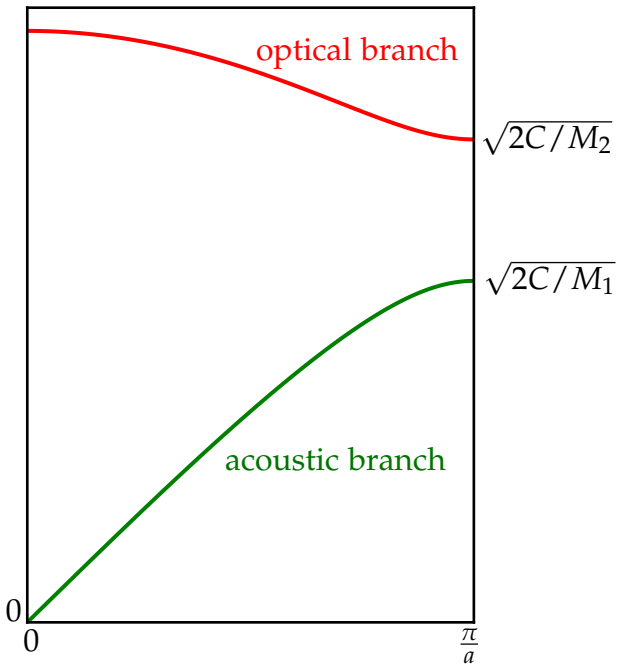

Figure 2.7: Dispersion relation for a linear chain of atoms with alternating masses M_1 and M_2, giving rise to a band gap and an optical branch.

to the dispersion relation of the mono-atomic case, whereas the optical branch shows a completely different behavior and has a finite energy at zero momentum. The band gap between the two branches is a result of their mass

difference and vanishes as the masses approach each other. Along with the vanishing band gap, the dispersion relation also reduces to the mono-atomic case, although with a different Brillouin zone boundary as the mass density is doubled compared to the original derivation (the lattice constant is now $a/2$ compared to the original value of a).

While the one dimensional case obviously does not fully represent the situation in the crystal, certain high symmetry directions can be considered as one dimensional problems. Other directions need a more complete treatment, including more neighboring atoms as well as different force constants depending on their distances. Also neglected so far is the polarization of the phonons, which gives rise to additional branches per polarization[14]. Finally, all those waves in the crystal correspond (in their description) to a harmonic oscillator, leading to a quantization of the energy

$$\epsilon = \left(n + \frac{1}{2}\right)\hbar\omega, \tag{2.15}$$

with n as the number of active phonons in this mode.

2.3.1 Surface Phonons

At the surface of the crystal the situation changes drastically. Due to the symmetry break new vibrational modes emerge[17,18]. Those modes are mostly confined to the surface, exhibiting wave-like properties parallel to the surface and decay rapidly inside the bulk. The new modes are called surface phonons, due to their localization to the surface. In addition to the surface localized modes there are many extra modes, which cannot be explained by a simple two dimensional oscillator model.

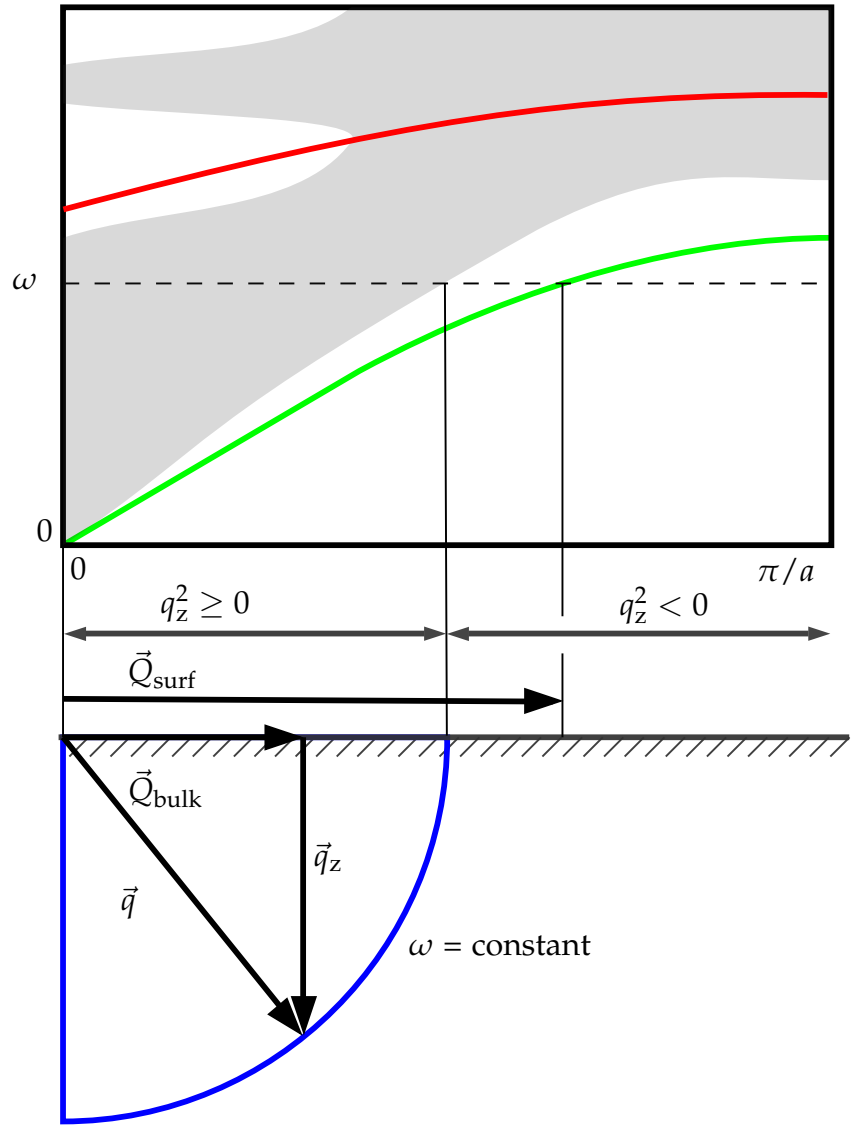

Figure 2.8: Schematic representation of a dispersion relation for surface phonons. They can be seen as a projection of the bulk modes onto the surface, leading to bulk bands (gray area) as long as $q_z^2 \geq 0$. The depicted colored modes originate purely from the two-dimensional surface as described in more detail in section 2.3.1.

The origin of these modes is easily understood with the help of figure 2.8: For one energy ω, there is a multitude of bulk phonon momenta $\mathbf{q}$ with this exact

energy and leading to multiple projections $\mathbf{Q}_{\text{bulk,i}}$ on the surface. Repeating this for multiple phonon energies results in bulk projected bands as depicted by the gray area in figure 2.8. The figure also shows modes which cannot originate from the bulk, as the surface wave vector $\mathbf{Q}_{\text{surf}}$ would be higher than the bulk wave vector $\mathbf{q}$. Those modes originate purely from the two-dimensional surface and are always lower than their corresponding bulk bands. This is a result of the alteration of the force constants between the atoms on the surface, as they have fewer neighbors than in the bulk. In general this leads to a softening of the modes[17].

2.4 Helium Atom Scattering from Surfaces

The first helium atom scattering experiments were performed on the (100) crystal face of lithium fluoride around 1930 by Estermann and Stern [19]. The experiment showed that it is possible to perform atom diffraction experiments if the *de Broglie* wavelength of the particle is in the order of the spacing between the surface atoms. Further measurements were complicated by the fact that the helium beam's velocity distribution was not narrow enough. This changed in the 1960s with the development of high pressure nozzles, allowing a quasi mono-energetic beam. Nowadays the beams are of such high quality that resolutions below one millielectron volt are achieved easily, which opened the path to measurements of surface phonons as described later in this thesis. Aside from the good resolution, HAS offers a few advantages over other surface investigation methods:

- The method is absolutely non-destructive due to the low energies used (roughly 15 to 45 meV in our experiments) and due to the classical turning

point being a few Ångström away from the core positions.

- Atom scattering, as opposed to neutron or electron scattering, is purely surface sensitive. The atoms only interact with the electron density distribution at the surface. As such any data gained about the bulk has to be coupled to the electron density oscillations on the surface in some way.
- The use of noble gases is of advantage due to their magnetic, electric and chemical inertness. Furthermore, due to their low natural occurrence, the detection becomes less complicated.

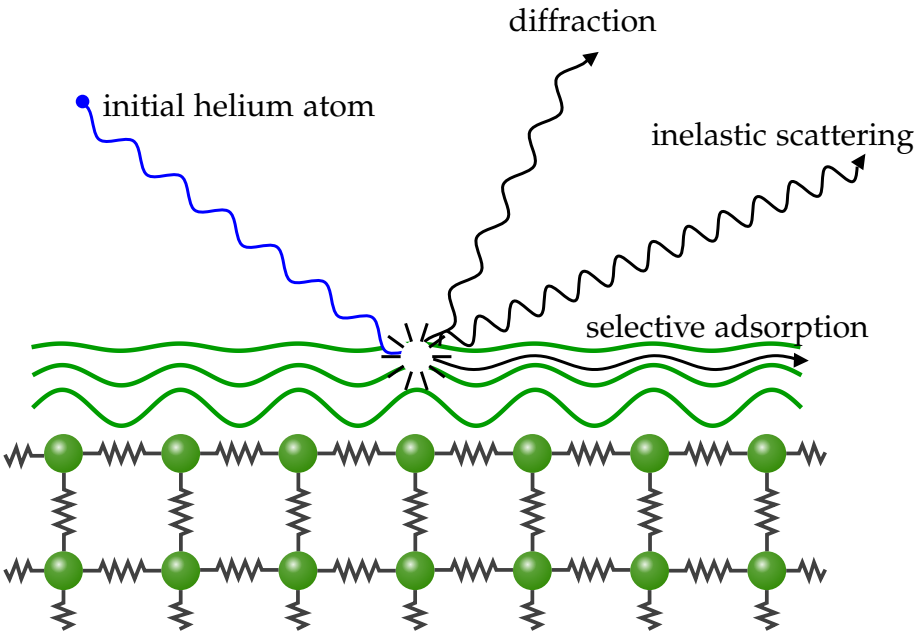

Figure 2.9: Graphical representation of the scattering mechanisms occurring in HAS.

This section will provide an overview over surface interaction potentials and the scattering mechanism occuring in HAS, figure 2.9 gives a simple graphical summary of those mechanisms. Furthermore, a quantum mechanical framework to calculate the scattering intensities is derived.

2.4.1 Interaction Potentials and Surface Corrugation

The interaction between the helium atom and the surface is described in detail in earlier literature[20,21,22,5], as such this section is just a short overview and the interested reader is referred to the existing material.

To obtain an interaction potential several simplifications are usually taken. First of all, the interaction between the helium atoms themselves, and their orientation is neglected. The potential is then written as $V(r, \{\mathbf{u}_i\})$ with $r = |\mathbf{r}|$ as the position of the helium atom and the set $\{\mathbf{u}_i\}$ of displacements of the surface atoms. To simplify the calculations further the thermal motion of the atoms is ignored. Finally the potential is written as a sum (or integral in the continuum model) of two-body potentials:

$$V(r) = \sum_i V(|\mathbf{r} - \mathbf{r}_i|). \tag{2.16}$$

Conceptually those two-body potentials consist of an attractive and repulsive part, as a consequence of the Van-der-Waals forces and the Pauli repulsion, respectively. Several choices exist for those potentials[23,24], with the Lennard-Jones (or 12-6) potential as one of the more popular choices:

$$V_{LJ}(r) = 4D\left[\left(\frac{\sigma}{r}\right)^{12} - \left(\frac{\sigma}{r}\right)^{6}\right]. \tag{2.17}$$

Here r is the distance between the two atoms, D is the well depth and σ is the equilibrium position. Since the position of the impinging atom with regard to the surface atoms is not known, it is easier to work with a surface averaged interaction potential instead. This is done in the continuum model where the crystal is assumed to be a homogeneous mass and the sum is exchanged with an integral, leading to an analytical solution, namely the 9-3 potential[23,25]:

$$V_{9-3}(z) = 3^{3/2}\frac{D}{2}\left[\left(\frac{\sigma}{z}\right)^{9} - \left(\frac{\sigma}{z}\right)^{3}\right]. \tag{2.18}$$

As the potential is laterally averaged only the normal distance z to the surface is relevant anymore; σ and D describe the same quantities as before.

Another commonly used potential, which is often chosen for its easy analytical accessibility[26], is the *Corrugated Morse potential*[27]:

$$V(\mathbf{R}, z) = D\left[\frac{1}{\mathcal{V}_0}\mathrm{e}^{-2\chi[z-\xi(\mathbf{R})]} - 2\mathrm{e}^{-\chi z}\right]. \tag{2.19}$$

Here, $\xi(\mathbf{R})$ is the corrugation function, χ the stiffness of the potential, and $\mathcal{V}_0$ the surface average of the exponential of the corrugation function,

$$\mathcal{V}_{\mathbf{G}} = \frac{1}{\Sigma}\int_{\Sigma}\mathrm{e}^{-\mathrm{i}\mathbf{G}\cdot\mathbf{R}}\mathrm{e}^{2\chi\xi(\mathbf{R})}\mathrm{d}\mathbf{R}, \tag{2.20}$$

evaluated at $\mathbf{G} = 0$. The corrugation function is defined as the locus of all turning points of the scattering process. It is highly dependent on the Bravais lattice and the lattice constants, as the position of the atoms strongly affects the electron density on the surface. Our samples possesses a hexagonal structure on the surface, leading to a corrugation as depicted in figure 2.10, calculated using

$$\begin{aligned}\xi(\mathbf{R}) = \xi_0 \cdot \Bigg[&\cos\left(\frac{2\pi}{a}\cdot\left(x - y/\sqrt{3}\right)\right) + \cos\left(\frac{2\pi}{a}\cdot\left(x + y/\sqrt{3}\right)\right) + \\ &+ \cos\left(\frac{2\pi}{a}\cdot\left(2y/\sqrt{3}\right)\right)\Bigg]\end{aligned} \tag{2.21}$$

as corrugation function, with a the lattice constant and ξ_0 the corrugation amplitude. One important aspect of the corrugated Morse potential is that its surface averaged potential is a standard Morse potential, allowing easy analytic calculation of its bound states, as well as the derivatives[26].

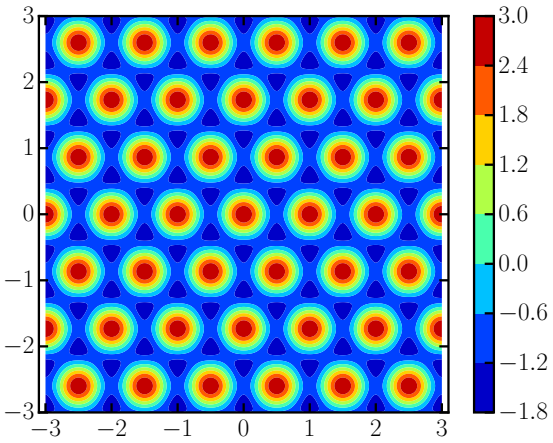

Figure 2.10: Example of the corrugation for a two dimensional hexagonal lattice. Red areas correspond to positions directly over the atomic cores, units are arbitrary.

2.4.2 Elastic Scattering

Scattering is considered elastic if the initial energy of the helium atom E_i is equal to the final energy E_f after the scattering event. Since the surface is periodic, the Laue equations can be used to derive conditions for the diffraction of incident waves by the crystal lattice. They state that the difference between the initial wave vector $\mathbf{k}_i$ and the final wave vector $\mathbf{k}_f$ has to be equal to the reciprocal lattice vector $\mathbf{g}$. Together with energy conservation this yields four equations:

$$E_f = E_i, \tag{2.22}$$

$$\mathbf{k}_f = \mathbf{k}_i + \mathbf{g}. \tag{2.23}$$

As HAS is surface sensitive the scattering only involves two-dimensional reciprocal lattice vectors. Following the common surface science nomenclature the wave vector $\mathbf{k} = (\mathbf{K}, k_z)$ is split into a two dimensional vector $\mathbf{K}$ residing

in the surface plane and a scalar k_z for the component normal to the surface. The direction perpendicular to the surface can be assumed to have infinite periodicity, leading to a relaxation of the Laue condition to

$$\Delta\mathbf{K} = \mathbf{K}_f - \mathbf{K}_i = \mathbf{G}_{h,k}. \tag{2.24}$$

A graphical interpretation of this condition is shown in figure 2.11.

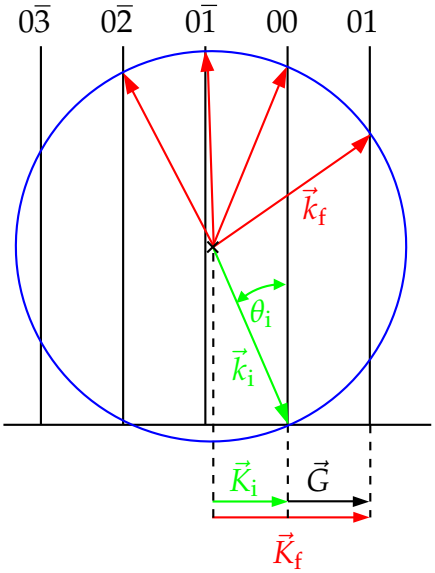

Figure 2.11: Construction of the Ewald sphere for two dimensions. Compared to the three dimensional case, the aperiodicity in the surface normal direction causes the lattice points to transform into rods, enabling a wider range of intersection possibilities. θ_i is the angle of incidence to the surface normal, the rest as described in the section.

2.4.3 HAS Peak Positions

Using the nomenclature from above it is possible to determine at which angles diffraction peaks occur. The following calculations assume *in-plane* diffraction, i.e. the wave vectors and surface normal are all in one plane. This is done since

the apparatus has source and detector arms in one plane, therefore in-plane diffraction will be assumed throughout the rest of this thesis unless noted otherwise. The energy conservation can be expressed as

$$0 = \Delta E = E_\mathrm{f} - E_\mathrm{i} = \frac{\hbar^2}{2m}\left(\mathbf{k}_\mathrm{f}^2 - \mathbf{k}_\mathrm{i}^2\right) \implies \mathbf{k}_\mathrm{f}^2 = \mathbf{k}_\mathrm{i}^2 \tag{2.25}$$

with m as the mass of the helium atom. Exploiting the in-plane diffraction, and further assuming that the initial wave vector is parallel to a reciprocal lattice vector, the parallel momentum transfer ΔK can be written in terms of the initial wave vector $k_\mathrm{i} = |\mathbf{k}_\mathrm{i}|$ and the scattering angles θ_i and θ_f:

$$\Delta K\left(\theta_\mathrm{i}\right) = k_\mathrm{i}\left(\sin\theta_\mathrm{f} - \sin\theta_\mathrm{i}\right). \tag{2.26}$$

By combining the previous equation with (2.24),

$$\theta_\mathrm{i} = \frac{\theta_\mathrm{SD}}{2} - \arcsin\left[\frac{G_\mathrm{hk}}{2k_\mathrm{i}\cos\frac{\theta_\mathrm{SD}}{2}}\right] \tag{2.27}$$

is derived, with $\theta_\mathrm{SD} = \theta_\mathrm{i} + \theta_\mathrm{f}$, the fixed source-detector angle. If the surface structure is known, θ_i can be calculated for a fixed energy k_i of the helium atom. In case the structure is not known yet, the measured position of the diffraction peaks can be used to extract G_hk.

2.4.4 Inelastic Scattering

While elastic scattering gives insight into the lattice structure, inelastic scattering can be used to obtain information about surface phonons and their dynamics. Helium atoms interacting with the surface can create or annihilate phonons and thereby loose or gain energy. This energy exchange results in a velocity change of the atoms, which can be measured at the detector. For simplicity and also because it is the most likely process for inelastic scattering only

single phonon events will be considered. As before, the energy and momentum of the system has to be conserved, leading to a set of three equations:

$$E_f = E_i + \Delta E \tag{2.28}$$

$$\mathbf{K}_f = \mathbf{K}_i + \Delta\mathbf{K}. \tag{2.29}$$

The parallel momentum transfer $\Delta\mathbf{K}$ splits into $\mathbf{G}_{h,k} + \mathbf{Q}$, where $\mathbf{Q}$ is the momentum of the created/annihilated phonon. By combining the two conservation laws, and assuming in-plane scattering, the energy ΔE of the phonon can be written as:

$$\Delta E = \hbar\omega(\Delta K) = \frac{\hbar^2}{2m}\left[\frac{k_i \cdot \sin(\theta_i) + \Delta K}{\sin(\theta_f)}\right]^2 - E_i. \tag{2.30}$$

This equation gives the energy for fixed initial conditions in dependence of the phonon momentum. Plotting this so called *scancurve* over a surface phonon dispersion relation, as shown in figure 2.12, will yield a few intersections which can be measured. To reach other phonons along the dispersion branches, either the angle of incidence or the initial energy of the helium atoms has to be changed.

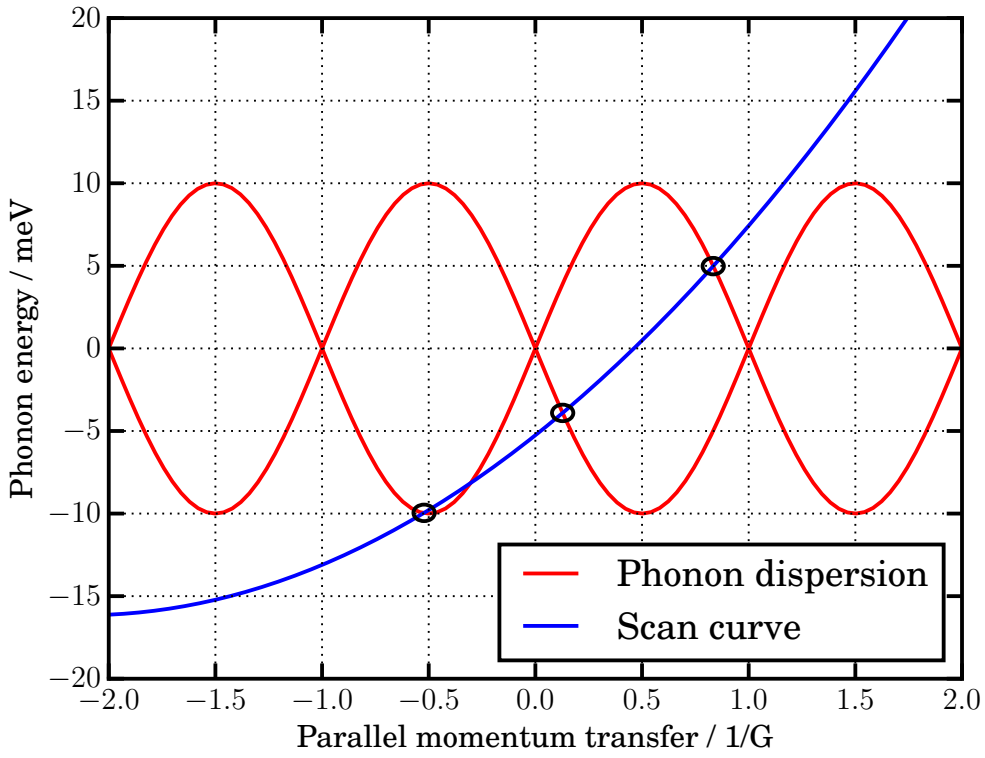

Figure 2.12: Scan curve for inelastic scattering processes. The blue line represents a scan curve and the red line is an approximation for a Rayleigh mode. Only at the marked intersections in black, scattering conditions are fulfilled. Changing either the angle or initial energy will move the scan curve slightly, which allows probing the whole dispersion relation in consecutive scans.

2.4.5 Calculation of Scattering Intensities

While the angular position of the diffraction peaks can be used to determine the lattice constants, the height of the peaks provides some insights into the surface corrugation. To calculate the intensities of the diffraction peaks a quantum mechanically complete approach, namely the Close-Coupling (CC) formalism, is applied. As first approximation the peaks can be seen as elastic effects,

therefore $\mathbf{Q} = 0$ and the Bragg condition simplifies to

$$\Delta\mathbf{K} = \mathbf{K}_f - \mathbf{K}_i = \mathbf{G}. \tag{2.31}$$

The time-independent Schrödinger equation which describes the scattering process is given by

$$\left[-\nabla^2 + V(\mathbf{r}) - \mathbf{k}_i^2\right]\Psi(\mathbf{r}) = 0, \tag{2.32}$$

with $\hbar^2/2m = 1$ to simplify the equations. Since the surface is assumed to be periodic, both the wave function Ψ and the interaction potential V can be written as Fourier series (following Sanz and Miret-Artés [22]):

$$\Psi(\mathbf{r}) = \sum_{\mathbf{G}} \Psi_{\mathbf{G}}(z) e^{i(\mathbf{K}_i + \mathbf{G})\cdot\mathbf{R}}, \tag{2.33}$$

$$V(\mathbf{r}) = \sum_{\mathbf{G}} V_{\mathbf{G}}(z) e^{i\mathbf{G}\cdot\mathbf{R}}. \tag{2.34}$$

By substituting equations (2.33) and (2.34) into equation (2.32), multiplying with the exponential of $-i(\mathbf{K}_i + \mathbf{G})\cdot\mathbf{R}$ and integrating over a single unit cell, a set of coupled equations is obtained:

$$\left[\frac{d^2}{dz^2} + \mathbf{k}_{\mathbf{G},z}^2 - V_{\mathbf{0}}(z)\right]\Psi_{\mathbf{G}}(z) = \sum_{\mathbf{G}'\neq\mathbf{G}} V_{\mathbf{G}-\mathbf{G}'}(z)\Psi_{\mathbf{G}'}(z). \tag{2.35}$$

Here, $V_{\mathbf{0}}(z)$ is the thermally and laterally averaged interaction potential (see section 2.4.1), and $\mathbf{k}_{\mathbf{G},z}^2$ gives the z-component of the diffracted wave:

$$\mathbf{k}_{\mathbf{G},z}^2 = \mathbf{k}_i^2 - (\mathbf{K}_i + \mathbf{G})^2. \tag{2.36}$$

Within this model, the Fourier coefficients $V_{\mathbf{G}-\mathbf{G}'}$ for a corrugated Morse potential are given by:

$$V_{\mathbf{G}-\mathbf{G}'} = D\frac{\mathcal{V}_{\mathbf{G}-\mathbf{G}'}}{\mathcal{V}_0} e^{-2\chi z}. \tag{2.37}$$

The CC-formalism then introduces the concept of diffraction channels, which are supported by an effective potential of the form $V_{\mathbf{0}}(z) + (\mathbf{K}_i + \mathbf{G})^2$, where

the addition to the bare potential can be viewed as the asymptotic energy[28] of the channel $\mathbf{G}$. Channels can be separated into *open* and *closed* ones. The classification is best described via a case analysis of $\mathbf{k}^2_{\mathbf{G},z}$, depending on whether the normal kinetic energy of the particle is above or below zero. In case of negative kinetic energies the impinging particle undergoes a transition into a bound state before leaving the surface again (more details in section 2.4.9). This leads to the following two cases:

- $\mathbf{k}^2_{\mathbf{G},z} \geq 0$: In this case the energy of the particle is above the asymptotic energy of the potential and as such in a classically allowed region. This case corresponds to *open* channels, usually written as $\left|\mathbf{K}_\mathrm{i} + \mathbf{G}, \mathbf{k}^2_{\mathbf{G},z}\right\rangle$.
- $\mathbf{k}^2_{\mathbf{G},z} < 0$: This area is classically forbidden and a particle is only allowed to enter this state if $\mathbf{k}^2_{\mathbf{G},z}$ is equal to the bound state energy ϵ_ν of the bare potential. The wave function can then be written as $|\mathbf{K}_\mathrm{i} + \mathbf{G}, \nu\rangle$ and the channel is said to be *closed*.

Equation (2.35) can be written in matrix form as

$$\frac{\mathrm{d}^2}{\mathrm{d}z^2}\mathcal{F} = \mathcal{W}(z)\mathcal{F}(z), \tag{2.38}$$

whereas the elements of those matrices are:

$$w_{\mathbf{G},\mathbf{G}'}(z) = -\mathbf{k}^2_{\mathbf{G},z}\delta_{\mathbf{G},\mathbf{G}'} + V_{\mathbf{G}-\mathbf{G}'}(z), \tag{2.39}$$

$$f_{\mathbf{G},\mathbf{G}'}(z) = \Psi_{\mathbf{G},\mathbf{G}'}(z). \tag{2.40}$$

By discretizing this system ($z_\mathrm{i} = z_0 + i \cdot h$, with i the running index and h the distance between the points) and applying Numerov's method a matrix version of the standard Numerov algorithm is obtained:

$$\left[\mathcal{I} - \frac{1}{12}h^2\mathcal{W}_{\mathrm{i}+1}\right]\mathcal{F}_{\mathrm{i}+1} + \left[\mathcal{I} - \frac{1}{12}h^2\mathcal{W}_{\mathrm{i}-1}\right]\mathcal{F}_{\mathrm{i}-1} - \left[\mathcal{I} + \frac{10}{12}h^2\mathcal{W}_\mathrm{i}\right]\mathcal{F}_\mathrm{i} \approx 0. \tag{2.41}$$

Here $\mathcal{I}$ is the identity matrix and the error per step is $\mathcal{O}(h^6)$. To solve this matrix equation the Fox-Goodwin algorithm[29] is used. A new matrix $\mathcal{R}$ is introduced which describes the propagation from $\mathcal{F}_i$ to $\mathcal{F}_{i+1}$.

$$\mathcal{F}_{i-1} = \mathcal{R}_{i-1}\mathcal{F}_i \tag{2.42}$$

$$\mathcal{F}_i = \mathcal{R}_i\mathcal{F}_{i+1} \tag{2.43}$$

Substituting equation (2.42) into equation (2.41) a recursive formula for the propagation matrices is derived,

$$\mathcal{R}_i = \left[\left[2\mathcal{I} + \frac{10}{12}h^2\mathcal{W}_i\right] - \left[\mathcal{I} - \frac{1}{12}h^2\mathcal{W}_{i-1}\right]\mathcal{R}_{i-1}\right]^{-1} \cdot \left[\mathcal{I} - \frac{1}{12}h^2\mathcal{W}_{i+1}\right]. \tag{2.44}$$

The whole system is solved by assuming the usual boundary conditions for the diffracted waves[22],

$$\mathcal{F}_i = \begin{pmatrix} Sin \\ 0 \end{pmatrix} + \begin{pmatrix} Cos & 0 \\ 0 & Exp \end{pmatrix} \cdot \begin{pmatrix} \mathcal{K} \\ \mathcal{E} \end{pmatrix} \tag{2.45}$$

with Sin, Cos restricted to the open channels and representing the incoming and outgoing waves:

$$Sin_{\mathbf{G},\mathbf{G}'} = \frac{1}{\sqrt{k_{\mathbf{G},z}}} \sin\left(k_{\mathbf{G},z} z_i\right) \delta_{\mathbf{G},\mathbf{G}'}, \tag{2.46}$$

$$Cos_{\mathbf{G},\mathbf{G}'} = \frac{1}{\sqrt{k_{\mathbf{G},z}}} \cos\left(k_{\mathbf{G},z} z_i\right) \delta_{\mathbf{G},\mathbf{G}'} \tag{2.47}$$

and Exp restricted to the closed channels with a decaying solution:

$$Exp_{\mathbf{G},\mathbf{G}'} = \frac{1}{\sqrt{|k_{\mathbf{G},z}|}} \exp\left(-|k_{\mathbf{G},z}| z_i\right) \delta_{\mathbf{G},\mathbf{G}'}. \tag{2.48}$$

$\mathcal{K}$ and $\mathcal{E}$ represent the channel intensities of the wave function. Given the framework above, it is easily possible to calculate the reaction matrix $\mathcal{K}$ from

equation (2.42). The overall intensities are then extracted from the scattering matrix $\mathcal{S}$ which is calculated via[30]:

$$\mathcal{S} = (1 - \mathrm{i}\mathcal{K})^{-1}(1 + \mathrm{i}\mathcal{K}). \tag{2.49}$$

The intensities are then given by

$$I_{\mathbf{G},\mathbf{0}} = |\mathcal{S}_{\mathbf{G},\mathbf{0}}|^2. \tag{2.50}$$

2.4.6 The Debye-Waller Factor

The close coupling calculations up to this point assumed that the atoms do not move. This is not the case for any real system, where the atoms undergo zero-point and thermal motions, resulting in inelastic scattering of the helium atoms. Due to the inelastic scattering, the scattering conditions for elastic diffraction is no longer fulfilled, leading to an attenuation of elastic scattering peaks and an increase of the signal in between them. To accommodate for this thermal attenuation, the so-called Debye-Waller factor[31] can be used to extrapolate from the intensity I_0 at zero Kelvin and a sample at rest to the intensity $I(T_\mathrm{S})$ of a sample at temperature T_S:

$$I(T_\mathrm{S}) = I_0 \mathrm{e}^{-2W(T_\mathrm{S})}. \tag{2.51}$$

Here, the exponential is the Debye-Waller factor and

$$W(T_\mathrm{S}) = \frac{1}{2}\left\langle (\mathbf{u}\cdot\mathbf{\Delta k}_\mathrm{i})^2 \right\rangle_\mathrm{T}. \tag{2.52}$$

The outer brackets are the thermal average, $\mathbf{u}$ is the displacement of the lattice atoms from their equilibrium position and $\mathbf{\Delta k}_\mathrm{i}$ refers to the momentum transfer from the scattering.

The Debye-Waller factor was initially proposed for x-ray and neutron diffraction, where interactions during the scattering event are short and weak. Since this does not hold for helium atom scattering, the above equations should not be trusted lightly. Nevertheless, they describe many experiments quite well, which justifies the use as first approximation before more accurate methods like inelastic close coupling calculations are required.

A simple expression for the Debye-Waller factor can be obtained by assuming that there is no parallel momentum transfer to the surface, simplifying equation (2.52) to:

$$W(T_S) = \left\langle u_z^2 \right\rangle \cdot (\Delta k_z)^2 . \tag{2.53}$$

Assuming a classical harmonic oscillator with frequency ω, the atomic displacement can be related to the temperature T_S via:

$$\frac{1}{2} M \omega^2 \left\langle u_z^2 \right\rangle = \frac{3}{2} k_B T_S \tag{2.54}$$

The mass of the surface atoms is given by M. Furthermore, by assuming the Debye model, the frequency ω can be written in terms of the surface Debye temperature θ_D:

$$\frac{\hbar \omega}{k_B T} = \frac{\theta_D}{T}. \tag{2.55}$$

Inserting those equations into equation (2.51), the final result

$$W(T_S) = \frac{3 \left(\hbar^2 \Delta k_z^2 \right) T_S}{2 M k_B \theta_D^2} \tag{2.56}$$

is obtained. Further improvements can be done by applying the Beeby correction as described in the doctoral thesis of Michael Mayrhofer-Reinhartshuber[4].

2.4.7 Extension to Inelastic Scattering

Depending on the sample and its direction, as well as the chosen potential, elastic CC calculations sometimes yield zero intensity for higher order diffraction peaks[6]. To achieve agreement with the measurements, a more complete approach, namely inelastic CC (*iCC*) has to be used. The term inelastic stems from the fact that phonon interactions are included in the model. As a first consequence of the lattice vibrations, the time-independent approach used before has to be dropped and the full time-dependent Schrödinger equation is employed to describe the interaction between the incoming particle and the surface:

$$\mathrm{i}\hbar\frac{\partial\Psi(\mathbf{r},t)}{\partial t} = \left[-\nabla^2 + V(\mathbf{r},t)\right]\Psi(\mathbf{r},t). \tag{2.57}$$

It stands to reason that the time dependence of the potential V arises through the position $\mathbf{R} + \mathbf{u}(\mathbf{R},t)$ of the atoms, where $\mathbf{u}(\mathbf{R},t)$ describes the displacement of atoms from their respective equilibrium positions. The displacement is conveniently described by[32]

$$\mathbf{u}(\mathbf{R},t) = \sum_{\mathbf{Q},\nu}\mathbf{A}\left(\mathbf{Q},\nu,T\right)\mathrm{e}^{\mathrm{i}\mathbf{Q}\cdot\mathbf{R}}\cos\left[\omega_\nu(\mathbf{Q})t\right], \tag{2.58}$$

with $\omega_\nu(\mathbf{Q})$ as the frequency in mode ν of a phonon with a parallel wave vector $\mathbf{Q}$. $\mathbf{A}\left(\mathbf{Q},\nu,T\right)$ describes the amplitude of this motion, including the phonon polarization vector and the dependence on the surface temperature T.

Since the displacement of the atoms is considered to be small compared to the lattice constant, a first order Taylor expansion is used to model the potential:

$$V(\mathbf{r},t) \approx V(\mathbf{R}) + \mathbf{u}(\mathbf{R},t)\cdot\nabla V(\mathbf{r}). \tag{2.59}$$

Due to the periodicity of the lattice, the potential can be written as Fourier series, in analogy to the elastic case. The same applies to the total wave function,

with the addition of a periodicity in time:

$$\Psi(\mathbf{r},t) = \mathrm{e}^{-\mathrm{i}\mathbf{k}_\mathrm{i}^2 t/\hbar}\Psi_{\mathbf{G}+\mathbf{Q},n_{\mathbf{Q},\nu}}(z)\mathrm{e}^{\mathrm{i}(\mathbf{K}_\mathrm{i}+\mathbf{G}+\mathbf{Q})\cdot\mathbf{R}}\mathrm{e}^{-\mathrm{i}n_{\mathbf{Q},\nu}\omega_\nu(\mathbf{Q})t}, \tag{2.60}$$

where $n_{\mathbf{Q},\nu}$ represents the number of phonons in the active mode. After inserting the Fourier series into the Schrödinger equation, multiplying with $\exp\left[-\mathrm{i}\left(\mathbf{K}_\mathrm{i}+\mathbf{G}+\mathbf{Q}\right)\right]$ as well as with $\exp\left[\mathrm{i}n_{\mathbf{Q},\nu}\omega_\nu(\mathbf{Q})t\right]$ and integrating over time and the area of a single unit cell, a set of coupled equations is obtained[22]:

$$\begin{aligned}
&\left[\frac{\mathrm{d}^2}{\mathrm{d}z^2} + \mathbf{k}^2_{\mathbf{G}+\mathbf{Q},n_{\mathbf{Q},\nu},z} - V_{\mathbf{0}}(z)\right]\Psi_{\mathbf{G}+\mathbf{Q},n_{\mathbf{Q},\nu}}(z)\\
&\quad= \sum_{\mathbf{G}'\neq\mathbf{G}} V_{\mathbf{G}-\mathbf{G}'}(z)\Psi_{\mathbf{G}'+\mathbf{Q},n_{\mathbf{Q},\nu}}(z)\\
&\quad+\frac{1}{2}\mathbf{A}(\mathbf{Q},\nu,T)\cdot\sum_{\mathbf{G}'}\left[\mathbf{F}_{\mathbf{G}-\mathbf{G}'-\mathbf{Q}}(z)+\mathbf{F}_{\mathbf{G}-\mathbf{G}'+\mathbf{Q}}(z)\right]\\
&\quad\times\left[\Psi_{\mathbf{G}+\mathbf{Q},n_{\mathbf{Q},\nu}+1}(z)+\Psi_{\mathbf{G}+\mathbf{Q},n_{\mathbf{Q},\nu}-1}(z)\right]
\end{aligned}$$

and

$$\begin{aligned}
&\left[\frac{\mathrm{d}^2}{\mathrm{d}z^2} + \mathbf{k}^2_{\mathbf{G}+\mathbf{Q},n_{\mathbf{Q},\nu}+1,z} - V_{\mathbf{0}}(z)\right]\Psi_{\mathbf{G}+\mathbf{Q},n_{\mathbf{Q},\nu}+1}(z)\\
&\quad= \sum_{\mathbf{G}'\neq\mathbf{G}} V_{\mathbf{G}-\mathbf{G}'}(z)\Psi_{\mathbf{G}'+\mathbf{Q},n_{\mathbf{Q},\nu}+1}(z)\\
&\quad+\frac{1}{2}\mathbf{A}(\mathbf{Q},\nu,T)\cdot\sum_{\mathbf{G}'}\left[\mathbf{F}_{\mathbf{G}-\mathbf{G}'-\mathbf{Q}}(z)+\mathbf{F}_{\mathbf{G}-\mathbf{G}'+\mathbf{Q}}(z)\right]\\
&\quad\times\left[\Psi_{\mathbf{G}+\mathbf{Q},n_{\mathbf{Q},\nu}+2}(z)+\Psi_{\mathbf{G}+\mathbf{Q},n_{\mathbf{Q},\nu}}(z)\right].
\end{aligned}$$

In the above equations

$$\mathbf{k}^2_{\mathbf{G}+\mathbf{Q},n_{\mathbf{Q},\nu},z} = \mathbf{k}_\mathrm{i}^2 - \left(\mathbf{K}_\mathrm{i}+\mathbf{G}+\mathbf{Q}\right)^2 - n_{\mathbf{Q},\nu}\hbar\omega_\nu(\mathbf{Q}) \tag{2.61}$$

is the kinetic energy component normal to the surface, and

$$\mathbf{F}_{\mathbf{G}-\mathbf{G}'\pm\mathbf{Q}}(z) \equiv \left[\mathrm{i}\left(\mathbf{G}-\mathbf{G}'\pm\mathbf{Q}\right)V_{\mathbf{G}-\mathbf{G}'\pm\mathbf{Q}}(z), V'_{\mathbf{G}-\mathbf{G}'\pm\mathbf{Q}}(z)\right] \tag{2.62}$$

is a vector function representing the perpendicular and normal force contributions from the gradient of the potential. Following the elastic case, open

and closed channels can be introduced once again, using the following notation: Open channels are written as $\left|\mathbf{K}_\mathrm{i}+\mathbf{G}+\mathbf{Q}, n_{\mathbf{Q},\nu}, \mathbf{k}^2_{\mathbf{G}+\mathbf{Q},n_{\mathbf{Q},\nu},\mathrm{z}}\right\rangle$ and closed channels are written as $|\mathbf{K}_\mathrm{i}+\mathbf{G}+\mathbf{Q}, n_{\mathbf{Q},\nu}, \nu\rangle$. In literature the channels are said to be *dressed* by the phonon field[33]. All channels within a single active mode form a so called *Floquet block*. In the case of single-phonon scattering, three Floquet blocks need to be considered: First a block dressed with zero phonons, which represents the elastic scattering contributions. The other two blocks, dressed with plus and minus one phonon respectively, stand for the creation and annihilation of phonons. Multi-phonon interactions are then achieved by adding more Floquet blocks on both sides as needed.

Care has to be taken about the coupling between the channels. The coupling factors are now split into *intrablock*, corresponding to the elastic coupling, and *interblock* couplings for the phonon interactions. Comparing the elastic and inelastic CC suggests that the scalar function

$$\mathbf{A}(\mathbf{Q},\nu,T)\cdot\mathbf{F}_{\mathbf{G}-\mathbf{G}'\pm\mathbf{Q}}(z) \tag{2.63}$$

is the *interblock* coupling and responsible for the thermal attenuation, which is otherwise approximated by the Debye-Waller factor.

To ease the calculations, a Debye model for the surface is assumed. Within this model, only the linear Rayleigh branch is considered, which usually exhibits a nearly shear-vertical character in the long wavelength limit. Exploiting this, the perpendicular components of $\mathbf{F}_{\mathbf{G}-\mathbf{G}'\pm\mathbf{Q}}(z)$ can be set to zero, simplifying the coupling to

$$\mathbf{A}(\mathbf{Q},\nu,T)\cdot\mathbf{F}_{\mathbf{G}-\mathbf{G}'\pm\mathbf{Q}}(z)\simeq A(\mathbf{Q},\nu,T)\cdot V'_{\mathbf{G}-\mathbf{G}'\pm\mathbf{Q}}(z). \tag{2.64}$$

The spatial derivative for the potential $V_{\mathbf{G}-\mathbf{G}'\pm\mathbf{Q}}(z)$ can often be calculated analytically for potentials like the (used) corrugated Morse potential. In principle

$A(\mathbf{Q}, \nu, T)$ as a whole would be a fitting parameter, but a simple form has been derived for copper surfaces[32], which has the benefit that it allows fitting the surface Debye temperature instead, in turn allowing easier comparison with previous results:

$$A(\mathbf{Q}, \nu, T) = \frac{1}{aQ_c}\sqrt{\frac{384\hbar^2\pi T}{Mk_B\Theta_D^2}} \tag{2.65}$$

Here, Q_c describes a cut-off factor for the harmonic movement. Till now, the calculations done throughout this work set the phonon momentum to zero. This is done as a first approximation, as the coupling factors have not yet been evaluated for phonons bearing momentum. Taking those limitations into account, it is possible to calculate scattering intensities in exactly the same way as in elastic scattering. The calculated intensities do not represent a measurable quantity, as it only includes a single phonon mode. To be able to compare with the measurable intensities it is necessary to include all modes within the selected phonon branch, that is integrate over all phonons weighted by their spectral density $\rho(\omega_\nu(\mathbf{Q}))$ up to the Debye frequency ω_D:

$$\langle I_{\mathbf{G}+\mathbf{Q}}\rangle = \int_0^{\omega_\mathrm{D}} I_{\mathbf{G}+\mathbf{Q},n_{\mathbf{Q},\nu}}\rho(\omega_\nu(\mathbf{Q}))\mathrm{d}\omega_\nu(\mathbf{Q}) \tag{2.66}$$

Within the Debye model, the two-dimensional spectral phonon density is

$$\rho(\omega) = \frac{3\omega}{\omega_\mathrm{D}^2}. \tag{2.67}$$

2.4.8 Implementation Considerations

To solve the above equations and calculate the scattering intensities, suitable channels and integration ranges have to be chosen. The number of channels has to be limited, since on one hand an infinite sum cannot be calculated unless one finds an analytical expression for it and on the other hand the calculation

time is of order $\mathcal{O}(N^3)$, with N being the number of included channels[34]. Open channels always have to be included completely since they are classically allowed. The number of closed channels usually depends on the corrugation, a higher corrugation results in larger coupling factors and therefore more channels have to be included[5]. The integration ranges are chosen according to the potential, starting way in the forbidden region so the wave function Ψ_G can be assumed to be zero and ending in the allowed region where the slope of the attractive potential is nearly zero[22].

2.4.9 Selective Adsorption Resonances and Resonance Lifetimes

Section 2.4.5 briefly touched selective adsorption resonances (SAR) while describing the concept of channels in close coupling calculations. This section is going to provide a deeper insight into SAR and their importance for HAS.

SAR have always been an area of great interest for HAS as they allow a better understanding of the gas-surface interactions near the surface[15,35,36]. Since they can affect the measured signals strongly, it is important to understand under which conditions they occur. Knowledge about their occurrence can then be used to enhance effects which would not be observable otherwise.

Although they can also manifest when phonon creation/annihilation is involved in the process, the following derivation only takes elastic scattering into account, extension to the inelastic case is trivial and does not change the concept behind it. More details about phonon assisted SAR can be found in the literature[37].

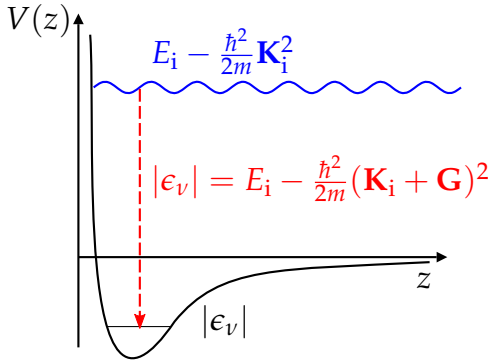

Figure 2.13: Illustration of selective adsorption process. An impinging atom is scattered into a bound state by taking up a surface **G**-vector. Its kinetic energy therefore increases from $\hbar^2\mathbf{K}_i^2/2m$ to $\hbar^2(\mathbf{K}_i + \mathbf{G})^2/2m$.

In the CC calculations, SAR appeared as part of the coupled equations. This section will revisit them from a simple kinematic point of view. SAR are only possible if the interaction potential supports bound states. If this is the case, the incident atom, under certain conditions, can be scattered into and get trapped in such a bound state. This situation is depicted in figure 2.13. A calculation of the total energy in this state yields

$$E_n(\mathbf{K}) = \frac{\hbar^2\mathbf{K}^2}{2m} - |\epsilon_\nu|, \tag{2.68}$$

with ϵ_ν as the energy of the bound state and $\mathbf{K}$ the wave vector of the atom on the surface. For a bound state to be involved in diffraction, two conservation laws have to be fulfilled. Energy conservation requires $E_n(\mathbf{K})$ to be equal to E_i or E_f. Furthermore the Laue condition has to be satisfied, so either $\mathbf{K}_i$ or $\mathbf{K}_f$ has to be equal to $\mathbf{K} \pm \mathbf{G}$ with $\mathbf{G} \neq 0$.

For purely elastic scattering, the atom enters a bound state and picks up $\mathbf{G}'$ in momentum, leading to $\mathbf{K} = \mathbf{K}_i + \mathbf{G}'$ and leaves the surface again during

interaction with $\mathbf{G}''$, leading to a final momentum of $\mathbf{K}_\mathrm{f} = \mathbf{K} - \mathbf{G}''$, so that

$$\mathbf{K}_\mathrm{f} = \mathbf{K}_\mathrm{i} + \mathbf{G}' - \mathbf{G}''. \tag{2.69}$$

This equation fulfills the Laue condition for the final as well as the initial state. Energy conservation for the elastic process requires $E_\mathrm{i} = E_\mathrm{n}(\mathbf{K}) = E_\mathrm{f}$ resulting in

$$\begin{aligned} E_\mathrm{i} &= \frac{\hbar^2}{2m}(k_\mathrm{i}\sin(\theta_\mathrm{i}) + G')^2 - |\epsilon_\nu| \\ &= \frac{\hbar^2}{2m}(k_\mathrm{f}\sin(\theta_\mathrm{f}) + G'')^2 - |\epsilon_\nu| = E_\mathrm{f}. \end{aligned} \tag{2.70}$$

Equation (2.70) allows the calculation of initial and final scattering angles under which the transition into a bound state is possible. From equation (2.69) it becomes evident, that a particle can either adsorb into a bound state or undergo direct scattering with a reciprocal lattice vector $\mathbf{G}' - \mathbf{G}''$ – the net result is the same, both leave the surface at the same angle and same energy. Quantum mechanically speaking, the only difference between the diffracted waves is a phase difference. This explains why the measured signal can contain maxima and minima when the conditions for bound state transitions are fulfilled, as the reflected particles interfere with each other.

In the presented model SAR are usually written as

$$\begin{pmatrix} G_1 & G_2 \\ & \nu \end{pmatrix}, \tag{2.71}$$

denoting the involved bound state ν and the initial reciprocal lattice vector $\mathbf{G}'$. An overview over all possible SAR including inelastic processes is depicted in Figure 2.14.

The time the helium atom is trapped on the surface can be seen as its lifetime. A higher lifetime can then lead to higher interaction probabilities with the

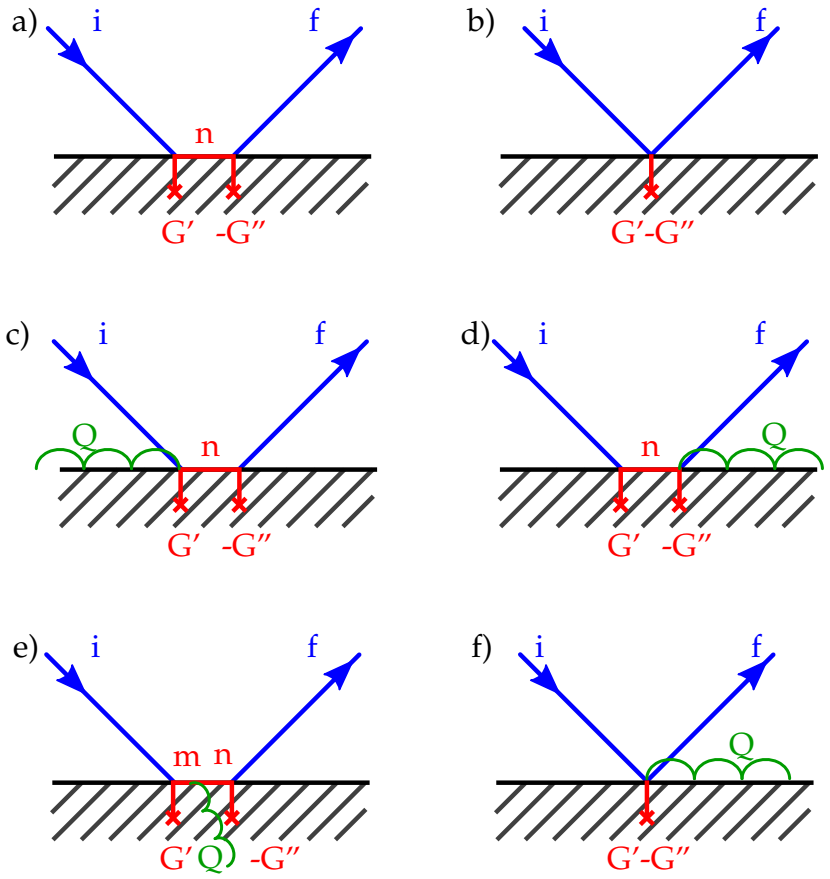

Figure 2.14: Diagram depicting all possible resonance types. (a) is the standard elastic scattering with bound state n. (c, d, e) depict inelastic scattering with bound state n. (b, f) are scatter processes in the specular channel.

surface electron cloud, resulting in an amplification of otherwise unobservable effects. To estimate the line widths, and from that the lifetimes, the *Fermi golden rule* can be used as a first approximation[38]. Within the golden rule treatment, the scattering process can be described as half a collision process, where the system is initially in the bound state ν of the closed channel $\mathbf{B}$ and then decays along all open diffraction channels $\mathbf{G}$[39]:

$$\Gamma^{(0)}_{\mathrm{B},\nu} = \pi \sum_{\mathbf{G}} \left| \left\langle \Psi^{(0)}_{\mathbf{G},\mathbf{k}^2_{\mathbf{B},\mathbf{G},z}} \middle| V_{\mathbf{B}-\mathbf{G}} \middle| \Psi^{(0)}_{\mathbf{B},\nu} \right\rangle \right|^2 , \tag{2.72}$$

with

$$\mathbf{k}^2_{\mathbf{B},\mathbf{G},z} = \epsilon^{(0)}_\nu + (\mathbf{K}_\mathrm{i} + \mathbf{B})^2 - (\mathbf{K}_\mathrm{i} + \mathbf{G})^2 \tag{2.73}$$

representing the relative kinetic energy between the closed channel **B** and one open channel **G**. The superscript in the above equations represent the zero order approximation when the full interaction potential is approximated by $V_0(z)$ and the other Fourier coefficients are seen as perturbation. An analytical expression for the linewidth was suggested by Hernández et al.[39] (the superscripts have been dropped for reading convenience):

$$\begin{aligned}\Gamma_{\mathrm{B},\nu} =& \pi \sum_{\mathbf{G}} \frac{2\gamma - 2\nu - 1}{64\nu!\Gamma(2\gamma - \nu)} \left| \frac{\mathcal{V}_{\mathbf{B}-\mathbf{G}}}{\mathcal{V}_0} \right|^2 \frac{\hbar^2\omega^2}{D} \\ &\times \frac{\sinh(2\pi\beta_\nu)}{\cosh^2(\pi\beta_\nu) - \cos^2(\pi(1/2+\gamma))} \\ &\times \left[(\gamma - \nu - 1/2) + \beta_\nu^2 + 2\gamma \right]^2 \\ &\times \left| \Gamma(1/2 + \gamma - \mathrm{i}\beta_\nu) \right|^2,\end{aligned} \tag{2.74}$$

with: $\omega = \chi(m/2D)^{-1/2}$, $\gamma = 2D/\hbar\omega$, $\beta_\nu = (\hbar\chi)^{-1}(2m\epsilon_\nu)^{1/2}$ and $\Gamma(k)$ the gamma function of k. Due to the finite number of open channels, the sum can be evaluated to get the line width and from there a mean value for the lifetime $\tau_{\mathbf{B},\nu}$ via the uncertainty principle:

$$\Gamma_{\mathbf{B},\nu}\tau_{\mathbf{B},\nu} \geq \hbar. \tag{2.75}$$

3 Experimental Setup

The apparatus used in our experiments was originally constructed at the FU Berlin and then moved to the Graz University of Technology. Its design is similar to most other HAS machines, therefore a detailed description can be found in literature[40,2] as well as in the doctoral thesis from Anton Tamtögl[21].

To be able to reach a good energetic resolution in the experiments, the helium beam needs to have a small energy spread. This is achieved by a supersonic expansion of the helium gas (He 6.0 at 50 bar) through a 10 µm nozzle into a low pressure chamber (base pressure $< 10^{-6}$ mbar). The central component of the beam is then selected with a skimmer to transfer only the laminar flow region into the next chamber. Depending on the temperature of the nozzle, which can be cooled down to 60 K and heated up to roughly 300 K, the helium atoms have a velocity between $v = 700\,\mathrm{m/s}$ and $v = 1700\,\mathrm{m/s}$ and a mean free path way above the apparatus dimensions. The velocity spread $\Delta v/v$ was calculated[21] to be roughly 1.5 %. After the skimmer a removable chopper disks splits the beam into small parts to allow time of flight analysis for inelastic measurements.

In the main chamber ultra high vacuum conditions are needed to keep the sample clean as long as possible (base pressure $< 10^{-10}$ mbar). The sample is mounted on a sample holder, which is attached to a 6-axes manipulator,

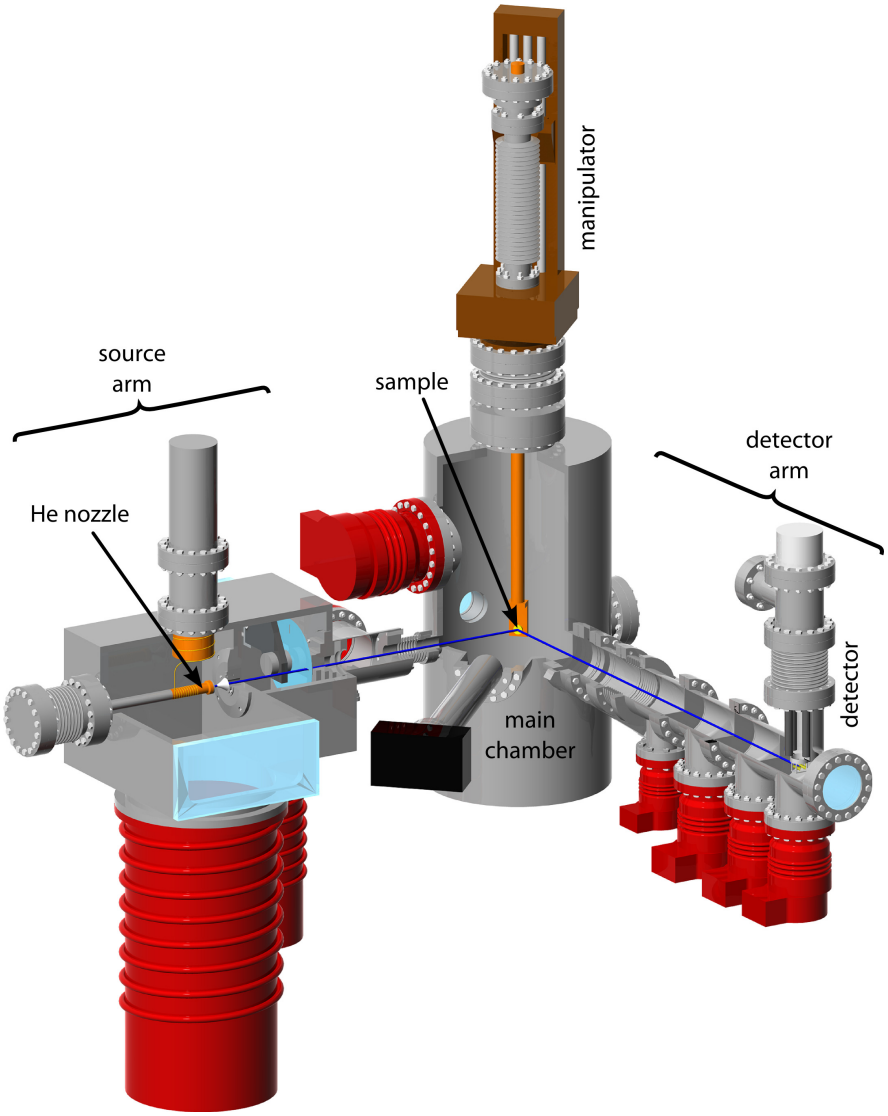

Figure 3.1: 3-dimensional CAD drawing[21] of the apparatus used in the experiments. The apparatus is divided in three separately pumped chambers, namely the source, main, and detection chamber. Red compartments symbolize the vacuum pumps and the blue line is the helium beam.

and can be cooled with liquid nitrogen to $-100\,°C$, or heated up using a button heater to $\approx 200\,°C$. Furthermore, the main chamber contains an Argon-

Ion sputter gun, to clean the sample, as well as a QMS (quadrupole mass spectrometer) for residual gas analysis and a combined AES/LEED (auger electron spectroscopy/low energy electron diffraction) for surface analysis.

The detector arm consists of several differentially pumped stages, separated by small apertures to only select directly scattered helium atoms and no background particles. Atoms passing through the whole arm are then ionized at the end and detected using a QMS with a home-made multi-channel analyzer (MCA). It is worth to note that the angle between the source and detector chamber is fixed to $\theta_{SD} = 91.5°$, resulting in fewer movable parts and easier vacuum setup, but making a few of the measurements cumbersome and others completely impossible.

This setup allows for several types of measurements which we categorize as elastic and inelastic measurements, even though our elastic measurements also include inelastic features. For the common elastic measurements, the energy of the helium atoms is kept constant and the incidence angle is swept through, resulting in diffraction patterns dependent on the crystal structure. A typical result of such a scan, including a more detailed description can be found in figure 3.2. For inelastic measurements the *time of flight* of the helium atoms is recorded, which allows to calculate their velocity and from there their kinetic energy, giving information on the energy loss or gain during the scattering process. Those energy changes can then be attributed to phonons and used to obtain information about the phonon dispersion relation on the surface. One inelastic result is depicted in figure 3.3.

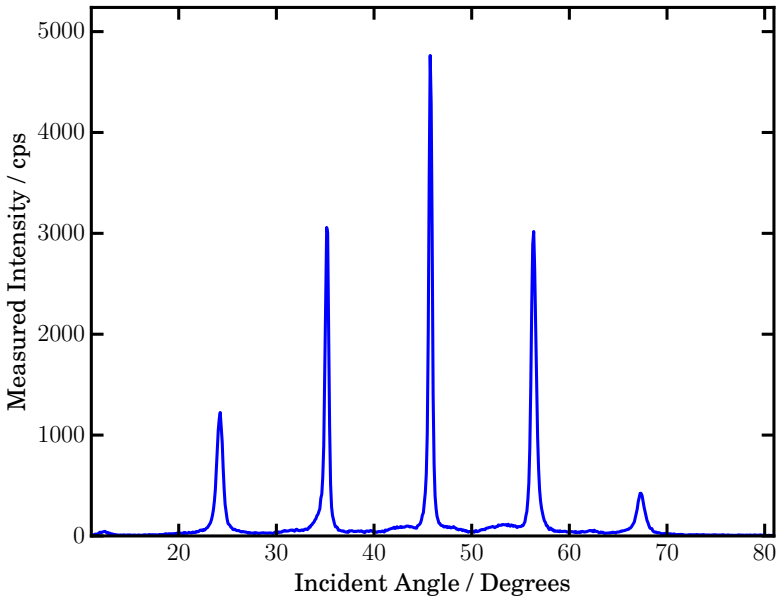

Figure 3.2: Typical angular scan in the $\overline{\Gamma K}$ direction. The specular peak is in the center and first and second order peaks are clearly visible. The background between those peaks is due to inelastic effects. The angular distance between the peaks allows determination of the crystal structure and lattice distances.

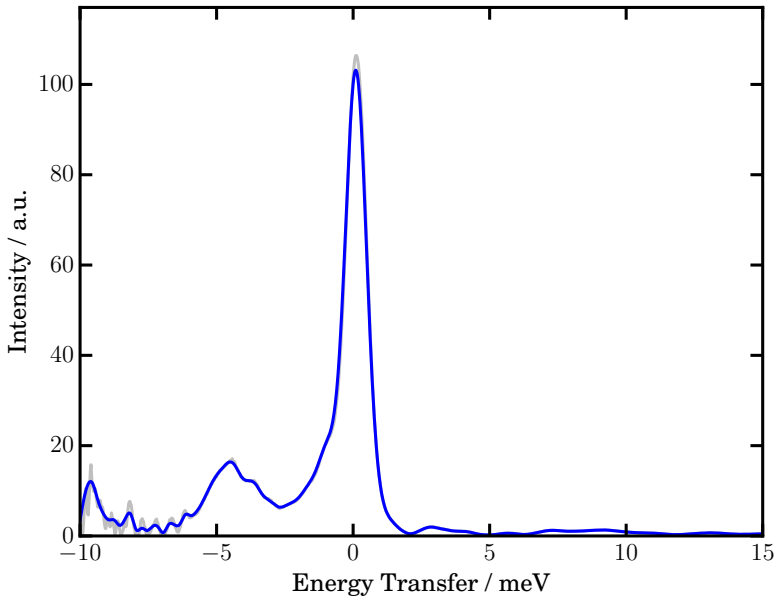

Figure 3.3: Exemplary *time of flight* measurement in the $\overline{\Gamma K}$ direction at 67.2 K. The large peak at 0 energy represents helium atoms which did not interact with any phonons. Peaks with a negative energy transfer indicate phonon creation events, in this case most likely on the Rayleigh mode.

4 Experimental Results

4.1 Measurement of SAR Lifetimes

Section 2.4.9 laid the ground work for SAR and provided an estimation for their lifetimes. In this section, line widths will be extracted from the measured drift spectra and compared to the theoretical results.

4.1.1 Measurements and Simulations

SAR can easily be measured by keeping all but one of the incidence parameters constant. For our drift spectra the temperature of the nozzle was varied and as such the energy of the incoming helium atoms. After cooling the sample to $-113\,^{\circ}\mathrm{C}$ and aligning the crystal in the $\overline{\Gamma\mathrm{M}}$ direction, the angles were fixed to the specular channel ($\theta_{\mathrm{SD}}/2$). Starting from a nozzle temperature of 57 K, one point was recorded every 0.25 K for a duration of 5 s by counting the number of helium atoms reaching the detector. The measurement was stopped at a temperature of 150 K. The raw results can be seen in figure 4.1.

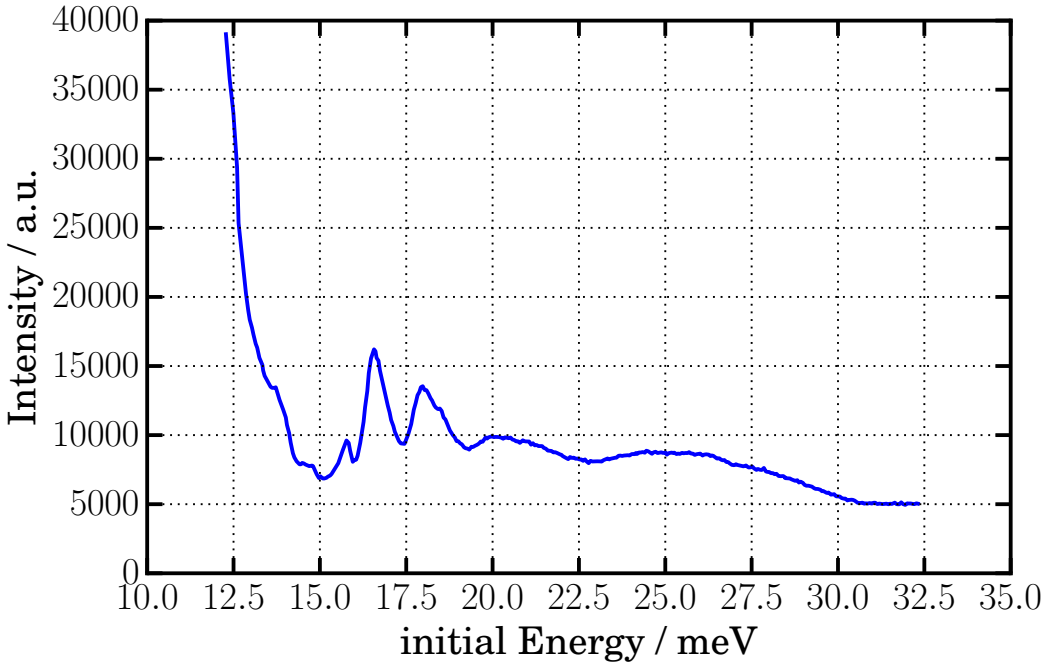

Figure 4.1: Drift spectra along the $\overline{\Gamma M}$ direction to allow the calculation of SAR lifetimes. The measured data shows three sharp peaks, as well as underlying oscillations from the surface structure.

Every 20 data points a time of flight spectrum was recorded, which allows a better determination of the helium energy than using the measured temperature of the nozzle. The raw data was then corrected using a linear model to account for the drift, the values for the measured temperatures as well as the quality of the fit can be found in figure 4.2. Unless otherwise noted, all calculations in this section are based on a Morse potential as central potential and the recently reported parameters for antimony from our group[5]. Given this preparation of the data, a simple kinematic analysis following equation (2.68) was carried out

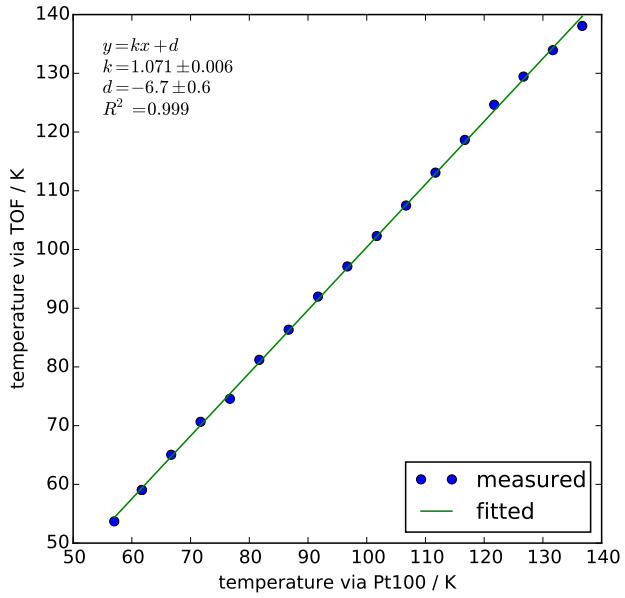

Figure 4.2: Linear fit to account for the temperature drift between the set value and the values obtained via the time of flight.

to get estimates for the SAR positions. The result can be found in figure 4.3. The figure also confirms that there are no critical values of incidence which could enhance resonance features strongly. This would be the case if the curve is tangent to the a bound state line[41]. A comparison of the intersections in figure 4.3 with figure 4.1 indicates that the highest three bound states are clearly visible in the drift spectrum. Simple kinematic calculations like these tend to ignore many effects like shifts in the peak positions due to band structure effects of the periodic potential the helium atom encounters on the surface[42]. Therefore eCC calculations have been carried out for the region of interest. As expected, they display a shift with regard to the kinematic conditions as shown in figure 4.4. An interesting aspect of the eCC calculations is the difference in the peak profiles, namely all resonances for the reciprocal lattice vector

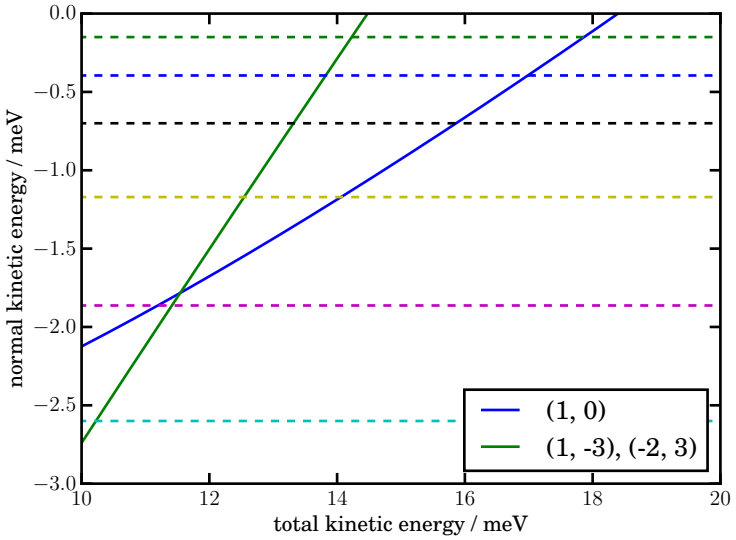

Figure 4.3: Simple kinematic analysis to assign the measured peaks to SAR. Dashed lines are the supported bound states of the interaction potential. Solid lines represent the normal kinetic energy of a helium atom after interacting with the respective reciprocal lattice vector. SAR are then possible at every intersection. It is important to note that due to symmetry considerations some of the lattice vectors are degenerate, even though the notation does not make this obvious immediately, but their distance to $(0,0)$ is the same.

$(1,0)$ appear to be of Lorentzian type, whereas the degenerate $(1,-3)$ and $(-2,3)$ channels manifest as Fano resonances. This appears to be a result of the degeneracy, although the coupling between these two channels is very weak and needs further work to confirm the origin of those shapes. For comparison the eCC calculations have also been carried out using a Hybrid Morse potential as central potential, leading to the results in figure 4.5. While the overall shape looks roughly the same, there are extra peaks around 14 meV and 18 meV which cannot be explained yet, hence the rest of the analysis will only consider the plain Morse potential.

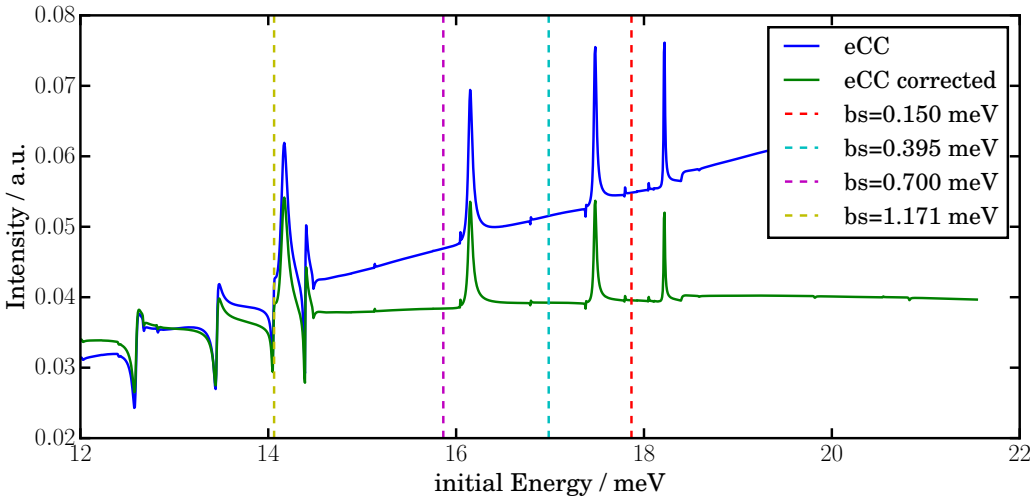

Figure 4.4: eCC calculations of the recorded drift spectrum. The blue line displays the raw results, the green line is corrected with the Debye Waller factor and a factor of $1/\sqrt{T}$ to account for the dropping nozzle intensity. Dashed lines represent the kinematic SAR positions for $\mathbf{G} = (1,0)$.

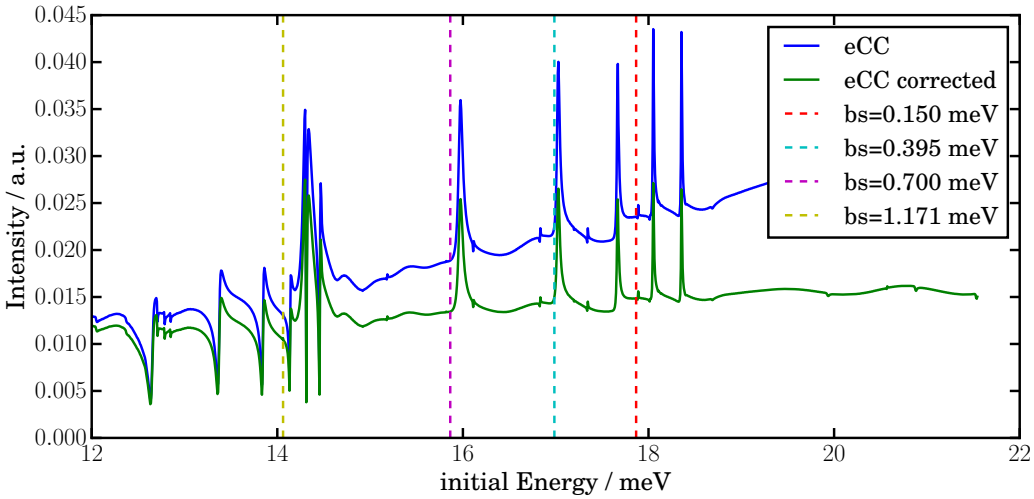

Figure 4.5: Same plot as figure 4.4 using a Hybrid Morse potential as central potential.

Table 4.1: Line widths and lifetimes of the SAR calculated using equation (2.74) and by fitting the peaks in the eCC calculations using Lorentz functions.

- $\mathbf{G}$ ... The reciprocal lattice vector the SAR corresponds to
- ν ... The quantum number of the bound state
- Γ ... The width (FWHM) in millielectronvolts calculated using Fermi's golden rule (equation (2.74))
- τ ... Lifetime in picoseconds, calculated via the uncertainty relation (equation (2.75))
- $\Gamma^{\text{int}}_{\text{eCC}}$ ... The internal width (FWHM) in millielectronvolts extracted from the eCC simulation
- τ_{eCC} ... Lifetime in picoseconds, calculated via the uncertainty relation (equation (2.75))

$\mathbf{G}$	ν	Γ/meV	τ/ps	$\Gamma^{\text{int}}_{\text{eCC}}$/meV	τ_{eCC}/ps
$(1,0)$	4	0.0140	46	0.0146 ± 0.0003	45.2 ± 0.8
$(1,0)$	5	0.0098	66	0.0089 ± 0.0002	74 ± 2
$(1,0)$	6	0.0043	151	0.0037 ± 0.0002	176 ± 8

4.1.2 Line Widths and Lifetimes

Section 2.4.9 covered the theoretical background for line widths, as well as their respective lifetimes. In this section the analytical line widths will be compared to line widths obtained from the eCC calculations and the measurements.

Evaluating equation (2.74) leads to a first estimate for the line widths as shown in table 4.1. In a similar fashion line widths from the eCC simulation, as well as the experiment, can be obtained by fitting the peaks to Lorentzian functions and extracting their full width at half maximum. The broadening of the peaks in the eCC simulations is a direct result of the coupling between

the diffraction channels and consequentially the corrugation and the surface structure. This is standing to reason when the effect of the corrugation on the interaction potential is considered. On a flat surface the interaction potential is independent of the lateral position of the helium atom, allowing it to travel in an equilibrium distance to the surface without any force influencing the helium atom. Contrary to that, a rough surface exhibits a constantly changing net force on the helium atom, allowing it to leave the surface (earlier) again. With this in mind, line widths have been extracted from the eCC simulations. Before those widths can be compared to the golden rule treatment, one further adjustment is needed: Intensity profiles, as observed in the experiment, are a function of scattering variables (incidence energy and angles) and not of the normal kinetic energy $\mathbf{k}^2_{\mathbf{G},z}$, which is the only variable representing the intrinsic properties of a resonance. Therefore two new types of variables are introduced: *external* and *internal*[22]. *External variables* are all variables which can be accessed and changed directly in the experiment. *Internal variables* on the other hand are the normal kinetic energies of the open and closed channels which depend on external variables. To convert external to internal variables a first order Taylor expansion can be used by keeping all but one of the experimental variables fixed and expanding around the SAR position[38]:

$$\Gamma^{\text{int}}_{\mathbf{G},\nu} = \left|\mathbf{k}^2_{\mathbf{G},z}(E \pm \Gamma^{\text{ext}}_{\text{E}}, \theta, \phi) - \epsilon_\nu\right| \tag{4.1}$$

$$\simeq \left|\left(\frac{\partial \mathbf{k}^2_{\mathbf{G},z}}{\partial E}\right)_{\text{E},\theta,\phi} \cdot \Gamma^{\text{ext}}_{\text{E}}\right|. \tag{4.2}$$

Using the formula above, line widths and lifetimes have been calculated for the eCC simulation, as displayed in table 4.1. They are in agreement with the simple analytical approach and increase for higher vibrational quantum numbers, which is expected as atoms in the lower states interact stronger with the corrugated part of the surface potential, forcing the atom to leave the

surface earlier[43].

When analyzing the measured data, it was first assumed that the three visible peaks between 15 meV and 20 meV would correspond to the bound state levels four to six. Overlaying the temperature corrected data with the eCC calculations as in figure 4.6 invalidated this assumption. The current hypothesis is, that the first peak is caused by kinematical focusing[44] with either the Rayleigh mode or an even lower lying plasmon mode. The shape of the peak does support this hypothesis and the effect would also explain why there is no corresponding peak in the eCC results. Nevertheless, confirmation of this theory has to wait until the inelastic measurements on antimony are fully analyzed.

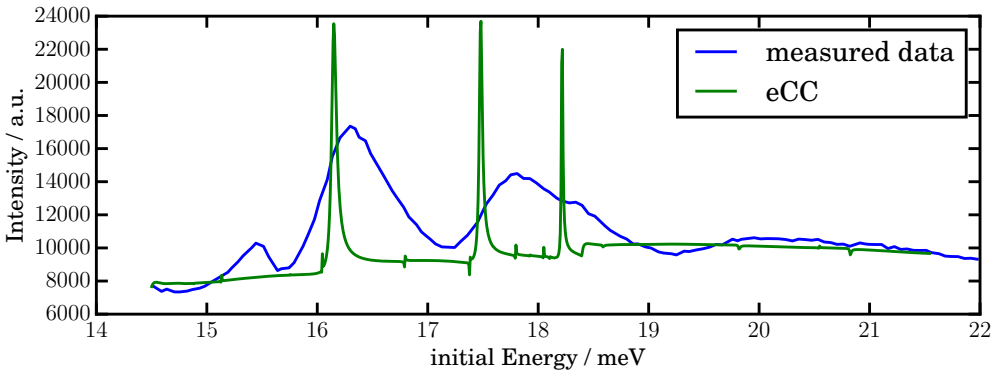

Figure 4.6: Comparison of the measured data with eCC calculations.

To obtain the line widths of the measured peaks, a proper fitting model has to be chosen. In general the peaks are expected to follow a Voigt profile, a convolution of a Lorentzian and a Gaussian, where the Gaussian is needed to account for the energy spread of the beam. Due to the complex background of the signal and the overlapping peaks, which makes the fitting cumbersome at best, the peaks were fitted using Gaussians to keep the parameter space

smaller. The background was also fitted using a broad Gaussian, which has no real counterpart, but at least allows a fit at all compared to an accurate background model including an exponential decay and overlayed oscillations for the surface terraces. Figure 4.7 shows the best fitting results obtained, the matching parameters can be found in table 4.2.

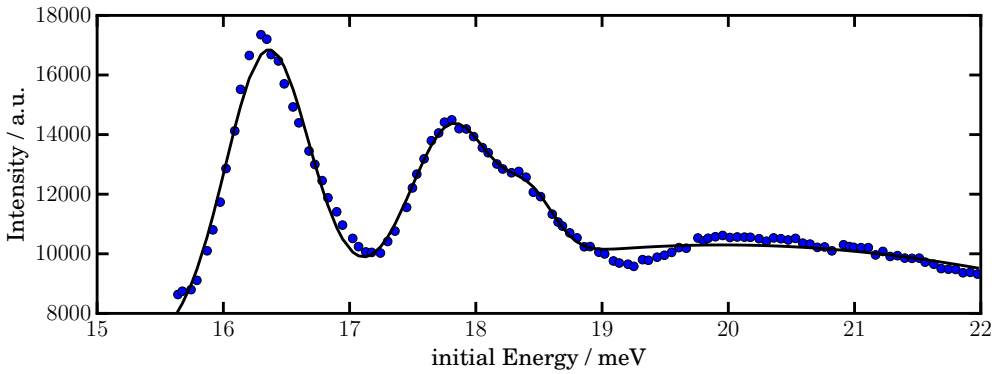

Figure 4.7: Best fitting results (black) for the measured data points (blue). Parameters can be found in table 4.2.

Table 4.2: Best fit parameters for the peaks from figure 4.7.

G ... The reciprocal lattice vector the SAR corresponds to

ν ... The quantum number of the bound state

E ... The position of the peak in millielectronvolts

A ... The amplitude of the Gaussian in arbitrary units

σ ... The standard deviation of the Gaussian in millielectronvolts

G	ν	E/meV	A/a.u.	σ/meV
$(1,0)$	4	16.348 ± 0.006	$7.3 \pm 0.4 \times 10^3$	0.33 ± 0.01
$(1,0)$	5	17.81 ± 0.02	$4.0 \pm 0.3 \times 10^3$	0.32 ± 0.02
$(1,0)$	6	18.44 ± 0.04	$8.4 \pm 2.5 \times 10^2$	0.20 ± 0.03

Before calculating the lifetimes from the fitted standard deviations two corrections have to be taken into account. The beam has an energy spread of $\Delta E/E \approx 1.5\%$ and is expected to exhibit a Gaussian character[21]. Since the convolution of two Gaussians is again a Gaussian, the new standard deviation can be easily calculated from $\sigma^2 = \sigma_1^2 + \sigma_2^2$. After deconvolution the internal linewidth has to be calculated as described by equation (4.1). The final results can be found in table 4.3.

It is clearly evident that the measured data and the theoretical models do not match. While the two theoretical models are in nearly perfect agreement, they ignore any inelastic effects, as well as scattering from defects, or, as in the case of the golden rule treatment, are only valid for weak corrugations. It therefore seems necessary to extend these models to inelastic (and possible even more) effects to accurately describe this type of experiments.

Table 4.3: Line widths and lifetimes for the SAR obtained from table 4.2.

G ... The reciprocal lattice vector the SAR corresponds to

ν ... The quantum number of the bound state

Γ_{ext} ... External line width in millielectronvolt

Γ_{int} ... Internal line width in millielectronvolt

τ ... Lifetime in picoseconds, calculated via equation (2.75) from the internal line width

G	ν	$\Gamma_{\text{ext}}/\text{meV}$	$\Gamma_{\text{int}}/\text{meV}$	τ/ps
$(1,0)$	4	0.70 ± 0.03	0.190 ± 0.008	3.5 ± 0.1
$(1,0)$	5	0.68 ± 0.06	0.19 ± 0.02	3.5 ± 0.3
$(1,0)$	6	0.3 ± 0.1	0.08 ± 0.04	8.2 ± 3.8

4.2 Environmental monitoring

The laboratory uses a custom monitoring application called *Oversight* to keep track of all the sensors. The goal of this section is to provide an overview over the architecture of this setup so it can be reproduced and changed easily. At the time of writing, this system aggregates data from ten sensors via *RS-232* serial connectors. The data is stored in a *SQLite* database with a time resolution of one minute and can be viewed via any Web browser. To ensure that measurements do not conflict with the monitoring, the system also provides an API which serializes concurrent requests to provide isolation. The application is currently accessible at `https://hesurfer.tugraz.at` and written in *Python* and *Django*. Figure 4.8 shows screenshots of the overview and detail pages.

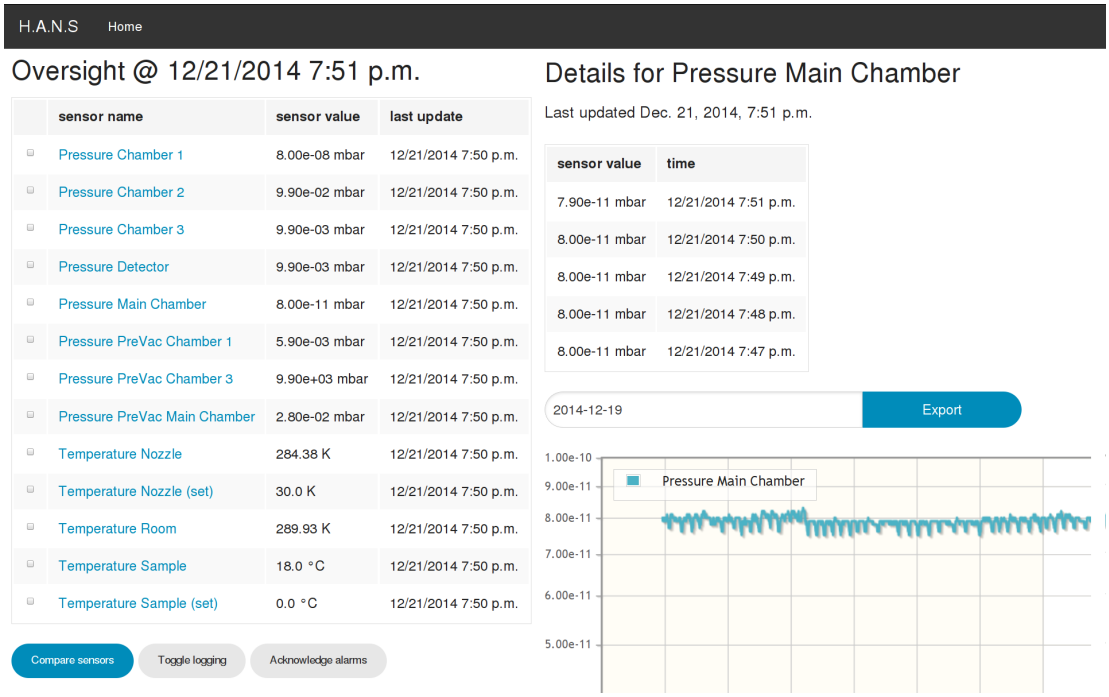

Figure 4.8: Screenshot of the overview and detail pages of *Oversight*.

4.2.1 Installation and Configuration

In its current form the system is meant to be installed on a *Raspberry Pi* (RPi) computer. As such the setup scripts assume a compatible configuration. The source code is hosted on *Github* and can be downloaded onto the local PC using *git*:

```
git clone https://github.com/apollo13/oversight
```

The folder *oversight* contains the actual source code and the folder *ansible* is used by the automation tool *Ansible* to configure a RPi which only needs to have *Debian* installed on it. Before the initial deployment can start, certain files need to be created, which are not in the repository for security reasons as they contain sensitive information like encryption keys. First of all, *Ansible* needs to know the hostname of the RPi. This information is usually contained in *ansible/hosts* under the section oversight:

```
[oversight]
hesurfer.tugraz.at
```

Oversight additionally needs some secret keys for security purposes, those are configured in *group_vars/oversight* which has to be a valid *YAML* file:

```
---
oversight_secret_key: <<insert 20 random alnum chars>>
oversight_api_key: <<insert 20 random alnum chars>>
ssl_privkey: |
  -----BEGIN RSA PRIVATE KEY-----
  <<insert x509 key>>
  -----END RSA PRIVATE KEY-----
```

```
ssl_pubkey: |
  -----BEGIN CERTIFICATE-----
  <<insert x509 key>>
  -----END CERTIFICATE-----
```

Once those files exist, the initial setup can be done by executing

```
ansible-playbook -t bootstrap,deployment site.yml
```

in the *ansible* folder. Subsequent runs can drop the bootstrap tag, so the deployment of new code will be faster.

4.2.2 Sensor Configuration

After logging in on the web page a link labeled *Admin* will take the user to the administration interface where users, groups and sensors can be edited, figure 4.9 shows the edit mask for sensors. The *name* and *unit* fields can be changed at will, while the *Api endpoint* should not change after initial creation (more details on the latter in the following section). Each sensor is represented by a Python class, which implements a *read* and *write* method and inherits *oversight.sensors.base.Sensor* for common functionality. The configuration of the sensor (for instance which serial port or the number of decimals) is done via the *Params* field in the admin. The data has to be a valid *JSON* object and the keys have to be supported by the constructor of the sensor class. The system currently supports temperature sensors via *Eurotherm* controllers which require the following configuration:

- Sensorclass: *oversight.sensors.eurotherm.EuroTherm*
- *port*: The serial port this device is attached to (eg. */dev/ttyUSB1*)

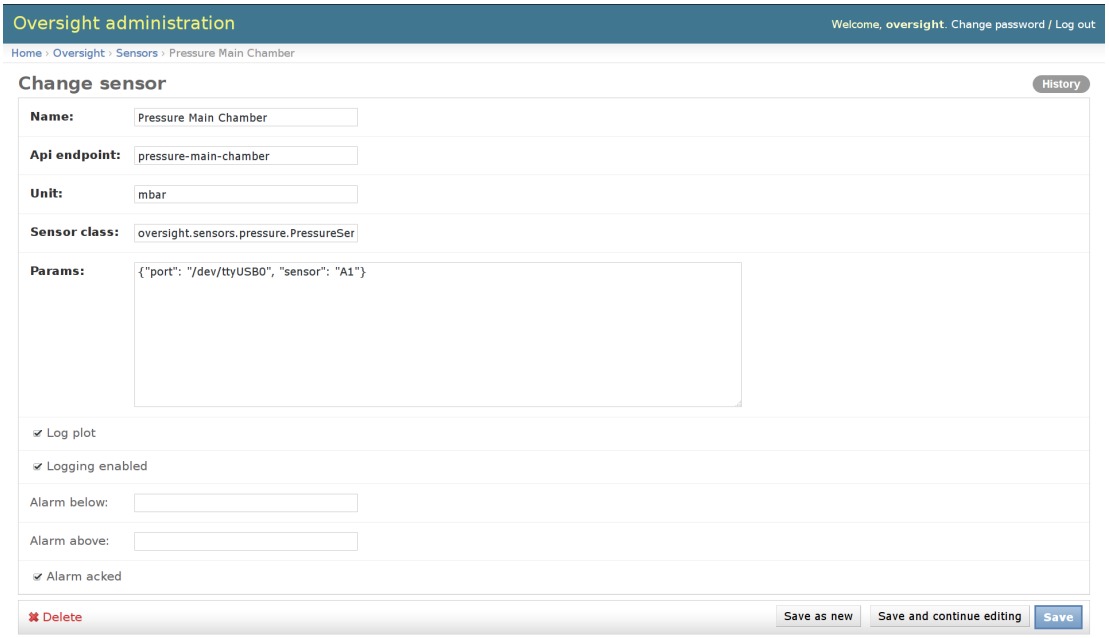

Figure 4.9: Screenshot of the admin page for sensors.

- *register*: The register on the controller, consult the controller's manual for register calculation.
- *number_of_decimals*: The controller returns numbers without decimal points depending on its configuration, this parameter can be used to readjust it to the correct number of decimals.

Pressure sensors are controlled via *Balzers TPG 300* controllers and are configured with:

- Sensorclass: *oversight.sensors.pressure.PressureSensor*
- *port*: The serial port this device is attached to (eg. */dev/ttyUSB1*)
- *sensor*: The sensor to read, as shown on the controller display (*A1* etc).

4.2.3 API Usage

The system provides access to the sensor data via an API, to allow other devices in the network to interact with it. *HTTPS* is used to secure the communication and a shared secret (namely *oversight_api_key* as configured earlier) is used to prevent unauthorized users from changing sensor values. The API is accessible under `https://hesurfer.tugraz.at/oversight/api/<endpoint>/<action>/`, where *endpoint* is the API endpoint configured in the admin interface and *action* currently is *read* or *write* (note that not all sensors/register support writing). The request to the endpoint must use the *POST*-method and has to include the shared secret as *api-key* and any arguments for the action as *args*. As an example, a request via curl to modify the configured nozzle temperature is shown:

```
curl -XPOST -d "api-key=<api_key>&args=59" \
<server>/oversight/api/temperatur-nozzle-set/write/
```

5 Summary and Discussion

During the course of this thesis, lifetimes of selective adsorption resonances on the He-Sb(111) system were measured and compared to two theoretical models.

As first approximation, a simple golden rule treatment as described in section 2.4.9 was used to obtain estimates for the order of magnitude of the lifetimes. This approach resulted in lifetimes between 46 ps and 151 ps. Additionally eCC calculations (figure 4.4 on page 47) in the area of interest have been carried out and lifetimes were extracted from the simulation. The results are in perfect agreement with the golden rule treatment as shown in table 4.1 on page 48.

When comparing the simulation with the actual measured data (as in figure 4.6 on page 50) it becomes evident that there is still a massive difference in the line widths and subsequently in the lifetimes. Part of this difference can be accounted for by taking the energy spread of the beam into account, but the lifetimes calculated from the measurement are still lower by a factor of ten to 20 (compare tables 4.1 and 4.3). One explanation could be that the current close coupling calculations do not consider inelastic effects (phonon creation and annihilation) since the inelastic parameters are not known yet for antimony. While this is true, Tuddenham et al. [45] found out that it should not affect the

widths of the features drastically. Instead, they suggest to use a potential with a corrugated attractive region as it should not affect the diffraction intensities but can change the signature of the features drastically[46].

Since our calculations already use a corrugated Morse potential, which exhibits this characteristic, it would be an interesting topic to reevaluate angular scattering spectra in conjunction with a drift spectra and different potentials, to not only account for the diffraction intensities but also for the signature of bound state resonances. So for now, the reported lifetimes should be taken as upper and lower boundaries and further work has to show if the experiment can be brought into concordance with an improved theory.

Last but not least, it should be mentioned that during the work on this thesis a new monitoring system was developed for the laboratory. It not only allows easier control of sensor data, but also provides better feedback in case of failures, including alarm functionality. The setup and configuration for this system can be found in section 4.2.

Bibliography

[1] Daniel Farias and Karl-Heinz Rieder. "Atomic beam diffraction from solid surfaces". In: *Reports on Progress in Physics* 61.12 (1998), p. 1575.

[2] J P Toennies. "Helium atom scattering: a gentle and uniquely sensitive probe of surface structure and dynamics". In: *Journal of Physics: Condensed Matter* 5.33A (1993), A25.

[3] M Mayrhofer-Reinhartshuber, A Tamtögl, P Kraus, and W E Ernst. "Helium atom scattering investigation of the Sb(111) surface". In: *Journal of Physics: Condensed Matter* 25.39 (2013), p. 395002.

[4] Michael Mayrhofer-Reinhartshuber. "Surface Structure and Dynamics of Bi(111) and Sb(111) from Helium Atom Scattering Experiments". PhD thesis. Graz University of Technology, 2013.

[5] Patrick Kraus, Michael Mayrhofer-Reinhartshuber, Christian Gösweiner, Florian Apolloner, Salvador Miret-Artés, and Wolfgang E. Ernst. "A comparative study of the He–Sb(111) interaction potential from close-coupling calculations and helium atom scattering experiments". In: *Surface Science* 630 (2014), pp. 208–215. ISSN: 0039-6028. DOI: 10.1016/j.susc.2014.08.007.

[6] M. Mayrhofer-Reinhartshuber, P. Kraus, A. Tamtögl, S. Miret-Artés, and W. E. Ernst. "Helium-surface interaction potential of Sb(111) from scattering experiments and close-coupling calculations". In: *Phys. Rev. B* 88 (20 Nov. 2013), p. 205425. DOI: 10.1103/PhysRevB.88.205425.

[7] Salvador Miret-Artés. "Elementary resonance processes in atom-surface scattering". In: *Surface Science* 366.2 (1996), pp. L735–L741. ISSN: 0039-6028. DOI: 10.1016/0039-6028(96)00936-3.

[8] G Benedek, P M Echenique, J P Toennies, and F Traeger. "Atoms riding Rayleigh waves". In: *Journal of Physics: Condensed Matter* 22.30 (2010), p. 304016.

[9] Patrick Kraus, Anton Tamtögl, Michael Mayrhofer-Reinhartshuber, Giorgio Benedek, and Wolfgang E. Ernst. "Resonance-enhanced inelastic He-atom scattering from subsurface optical phonons of Bi(111)". In: *Phys. Rev. B* 87 (24 June 2013), p. 245433. DOI: 10.1103/PhysRevB.87.245433.

[10] D. Hsieh, Y. Xia, L. Wray, D. Qian, A. Pal, J. H. Dil, J. Osterwalder, F. Meier, G. Bihlmayer, C. L. Kane, Y. S. Hor, R. J. Cava, and M. Z. Hasan. "Observation of Unconventional Quantum Spin Textures in Topological Insulators". In: *Science* 323.5916 (2009), pp. 919–922. DOI: 10.1126/science.1167733.

[11] Haijun Zhang, Chao-Xing Liu, Xiao-Liang Qi, Xi Dai, Zhong Fang, and Shou-Cheng Zhang. "Topological insulators in Bi2Se3, Bi2Te3 and Sb2Te3 with a single Dirac cone on the surface". In: *Nat Phys* 5.6 (June 2009), pp. 438–442. ISSN: 1745-2473. DOI: 10.1038/nphys1270.

[12] PengFei Zhang, Zheng Liu, Wenhui Duan, Feng Liu, and Jian Wu. "Topological and electronic transitions in a Sb(111) nanofilm: The interplay

between quantum confinement and surface effect". In: *Phys. Rev. B* 85 (20 May 2012), p. 201410. DOI: 10.1103/PhysRevB.85.201410.

[13] Feng-Chuan Chuang, Chia-Hsiu Hsu, Chia-Yu Chen, Zhi-Quan Huang, Vidvuds Ozolins, Hsin Lin, and Arun Bansil. "Tunable topological electronic structures in Sb(111) bilayers: A first-principles study". In: *Applied Physics Letters* 102.2, 022424 (2013). DOI: 10.1063/1.4776734.

[14] C. Kittel. *Introduction to Solid State Physics*. Wiley, 2004. ISBN: 978-0-4714-1526-8.

[15] N. Cabrera, V. Celli, F.O. Goodman, and R. Manson. "Scattering of atoms by solid surfaces. I". In: *Surface Science* 19.1 (1970), pp. 67–92. ISSN: 0039-6028. DOI: 10.1016/0039-6028(70)90111-1.

[16] C. S. Barrett, P. Cucka, and K. Haefner. "The crystal structure of antimony at 4.2, 78 and 298° K". In: *Acta Crystallographica* 16.6 (June 1963), pp. 451–453. DOI: 10.1107/S0365110X63001262.

[17] F.W. de Wette. "Study of Surface Phonons by the Slab Method". English. In: *Surface Phonons*. Ed. by Winfried Kress and FrederikW. de Wette. Vol. 21. Springer Series in Surface Sciences. Springer Berlin Heidelberg, 1991, pp. 67–109. ISBN: 978-3-642-75787-7. DOI: 10.1007/978-3-642-75785-3_4.

[18] Klaus Kern and George Comsa. "Helium-Scattering Studies of the Dynamics and Phase Transitions of Surfaces". In: *Advances in Chemical Physics*. John Wiley & Sons, Inc., 2007, pp. 211–280. ISBN: 978-0-470-14125-0. DOI: 10.1002/9780470141250.ch5.

[19] I. Estermann and O. Stern. "Beugung von Molekularstrahlen". German. In: *Zeitschrift für Physik* 61.1-2 (1930), pp. 95–125. ISSN: 0044-3328. DOI: 10.1007/BF01340293.

[20] Patrick Kraus. "Measurements of the He-Bi(111) Interaction Potential using Elastic helium atom scattering". MA thesis. Graz University of Technology, 2011.

[21] Anton Tamtögl. "Surface Dynamics and Structure of Bi(111) from Helium Atom Scattering". PhD thesis. Graz University of Technology, 2012.

[22] A.S. Sanz and S. Miret-Artés. "Selective adsorption resonances: Quantum and stochastic approaches". In: *Physics Reports* 451.2–4 (2007), pp. 37–154. ISSN: 0370-1573. DOI: 10.1016/j.physrep.2007.08.001.

[23] H. Hoinkes. "The physical interaction potential of gas atoms with single-crystal surfaces, determined from gas-surface diffraction experiments". In: *Rev. Mod. Phys.* 52 (4 Oct. 1980), pp. 933–970. DOI: 10.1103/RevModPhys.52.933.

[24] E. Hulpke, ed. *Helium Atom Scattering from Surfaces*. Springer-Verlag, 1992. ISBN: 978-3-6420-8115-6.

[25] Milton W. Cole and T.T. Tsong. "Bound state vibrational spectrum of the 3–9 atom-surface interaction". In: *Surface Science* 69.1 (1977), pp. 325–335. ISSN: 0039-6028. DOI: 10.1016/0039-6028(77)90177-7.

[26] Patrick Kraus. "Classical and quantum-mechanical atom-surface interaction models applied to He-scattering measurements on Bi(111) and Sb(111) surfaces". PhD thesis. Graz University of Technology, 2014.

[27] Armand, G. and Manson, J.R. "Scattering of neutral atoms by a periodic potential : the Morse corrugated potential". In: *J. Phys. France* 44.4 (1983), pp. 473–487. DOI: 10.1051/jphys:01983004404047300.

[28] M. Hernández, O. Roncero, S. Miret–Artés, P. Villarreal, and G. Delgado–Barrio. "Study of the diffraction mediated selective adsorption through the close–coupling and diabatic distorted wave formalisms. Application

to the 4He–Cu(110) system". In: *The Journal of Chemical Physics* 90.7 (1989), pp. 3823–3830. DOI: 10.1063/1.455839.

[29] L. Fox. *The Numerical Solution of Two-point Boundary Value Problems*. Oxford University Press, 1957. ISBN: 978-0-4866-6495-8.

[30] J.R. Taylor. *Scattering Theory*. John Wiley, New York, 1972. ISBN: 0-471-84900-6.

[31] S.V. Krishnaswamy, G. Derry, D. Wesner, T.J. O'gorman, and D.R. Frankl. "Debye-Waller effects in atom-surface scattering". In: *Surface Science* 77.3 (1978), pp. 493–504. ISSN: 0039-6028. DOI: 10.1016/0039-6028(78)90135-8.

[32] S. Miret-Artés. "Resonant inelastic scattering of atoms from surfaces". In: *Surface Science* 339.1–2 (1995), pp. 205–220. ISSN: 0039-6028. DOI: 10.1016/0039-6028(95)00632-X.

[33] Salvador Miret-Artés, Osman Atabek, and André D. Bandrauk. "Multiphoton absorption line shapes and branching ratios in intense laser fields: An application to H_2^+ photodissociation". In: *Phys. Rev. A* 45 (11 June 1992), pp. 8056–8063. DOI: 10.1103/PhysRevA.45.8056.

[34] R Martínez-Casado, B Meyer, S Miret-Artés, F Traeger, and Ch Wöll. "Diffraction patterns of He atoms from the MgO(100) surface calculated by the close-coupling method". In: *Journal of Physics: Condensed Matter* 19.30 (2007), p. 305006.

[35] H Chow and E.D Thompson. "Diffraction and selective adsorption in the corrugated hard wall model". In: *Surface Science* 54.2 (1976), pp. 269–292. ISSN: 0039-6028. DOI: 10.1016/0039-6028(76)90225-9.

[36] V. Celli, N. Garcia, and J. Hutchison. "Interpretation of selective adsorption in atom-surface scattering". In: *Surface Science* 87.1 (1979), pp. 112–128. ISSN: 0039-6028. DOI: 10.1016/0039-6028(79)90173-0.

[37] P. Cantini, G. P. Felcher, and R. Tatarek. "Inelastic Resonant Transitions of Atoms on a LiF Surface". In: *Phys. Rev. Lett.* 37 (10 Sept. 1976), pp. 606–609. DOI: 10.1103/PhysRevLett.37.606.

[38] M. Hernández, S. Miret-Artés, P. Villarreal, and G. Delgado-Barrio. "Study of the selective adsorption phenomenon in the 4He/Cu(11a) (with a = 0, 3, 5, 7) elastic scattering: the critical kinematic effect". In: *Surface Science* 274.1 (1992), pp. 21–34. ISSN: 0039-6028. DOI: 10.1016/0039-6028(92)90096-O.

[39] M. Hernández, S. Serna, O. Roncero, S. Miret-Artés, P. Villarreal, and G. Delgado-Barrio. "Time-dependent golden rule treatment of the He-Cu(110) elastic scattering". In: *Surface Science* 251–252 (1991), pp. 373–376. ISSN: 0039-6028. DOI: 10.1016/0039-6028(91)91017-R.

[40] T. Engel and K.H. Rieder. "Structural studies of surfaces with atomic and molecular beam diffraction". English. In: *Structural Studies of Surfaces*. Vol. 91. Springer Tracts in Modern Physics. Springer Berlin Heidelberg, 1982, pp. 55–180. ISBN: 978-3-540-10964-8. DOI: 10.1007/BFb0041342.

[41] M. Hernández, S. Miret-Artés, P. Villarreal, and G. Delgado-Barrio. "Enhancement of resonance features at critical values of the incidence parameters in gas atom-surface elastic scattering; The 4He-Cu(110) example". In: *Surface Science* 251–252 (1991), pp. 369–372. ISSN: 0039-6028. DOI: 10.1016/0039-6028(91)91016-Q.

[42] G. Armand and J.R. Manson. "An exact iterative solution of the atom-surface scattering problem for realistic potentials". In: *Surface Science* 119.1

(1982), pp. L299–L306. ISSN: 0039-6028. DOI: 10.1016/0039-6028(82)90171-6.

[43] G. Brusdeylins, R. Bruce Doak, and J. Peter Toennies. "Observation of selective desorption of one–phonon inelastically scattered He atoms from a LiF crystal surface". In: *The Journal of Chemical Physics* 75.4 (1981), pp. 1784–1793. DOI: 10.1063/1.442257.

[44] G. Benedek, G. Brusdeylins, J. P. Toennies, and R. B. Doak. "Experimental evidence for kinematical focusing in the inelastic scattering of helium from the NaF(001) surface". In: *Phys. Rev. B* 27 (4 Feb. 1983), pp. 2488–2493. DOI: 10.1103/PhysRevB.27.2488.

[45] F E Tuddenham, H Hedgeland, J Knowling, A P Jardine, D A MacLaren, G Alexandrowicz, J Ellis, and W Allison. "Linewidths in bound state resonances for helium scattering from Si(111)–(1 × 1)H". In: *Journal of Physics: Condensed Matter* 21.26 (2009), p. 264004.

[46] J. R. Manson and K.-H. Rieder. "Eikonal approximation in atom-surface scattering: Effects of a corrugated attractive well". In: *Phys. Rev. B* 62 (19 Nov. 2000), pp. 13142–13146. DOI: 10.1103/PhysRevB.62.13142.

Acknowledgments

First of all I have to thank my supervisor Prof. Wolfgang E. Ernst for giving me the possibility to write my thesis at his institute, as well as his enduring support and help during this year. I also want to thank Prof. Salvador Miret-Artès whose expertise was needed for many parts of this thesis and his patience in answering my infinite stream of e-mails (to be honest: I stopped counting them).

When it comes to colleagues one cannot wish for anyone else but Christian Gösweiner, Patrick Kraus, and Michael Mayrhofer-Reinhartshuber. Thanks to them, work was a joy every day, no matter how much was broken or how many bugs the algorithms still had. To add to this joy, our office was constantly under siege by Michael Hollerer and Bernhard Krenmayer.

In addition to the mentioned friends I would like to thank everyone from the roof terrace of our dormitory, be it an ordinary barbeque or highly philosophical discussions during mild summer nights; it would not have been the same without all of you! With this year being one hell of a ride, I especially want to thank Johanna Kortschak for the fun we had and her support and encouragement when everything else seemed to fail.

Above them all I would like to thank my parents, Maria and Udo, and my brother Peter – without them I would have never gotten this far.